Current motion and deformation of the Nazca Plate: new constraints from GPS measurements

Paul Jarrin, Jean-Mathieu Nocquet, Frédérique Rolandone, H. Mora-Páez, P.
Mothes, D. Cisneros

Current motion and deformation of the Nazca Plate: new constraints from GPS measurements

P. Jarrin [1] J.-M. Nocquet [2,3] F. Rolandone [1] H. Mora-Páez [4] P. Mothes [5] and D. Cisneros[6]

[1]*Sorbonne Université, CNRS-INSU, Institut des Sciences de la Terre Paris, ISTeP, UMR 7193, F-75005 Paris, France. E-mail:* paulalbertoj@gmail.com
[2]*Université Côte d'Azur, IRD, CNRS, Observatoire de la Côte d'Azur, Géoazur, 06560 Valbonne, France*
[3]*Université Paris Cité, Institut de Physique du Globe de Paris, 75005 Paris, France*
[4]*Colombian Geological Survey, Space Geodesy Research Group, Bogotá 111321, Colombia*
[5]*Escuela Politécnica Nacional Instituto Geofísico, Ladrón de Guevara E11-253 Apartado, 2759 Quito, Ecuador*
[6]*Instituto Geográfico Militar de Ecuador, Sector El Dorado, 2435 Quito, Ecuador*

SUMMARY

We use new GPS data to determine an updated Euler pole describing the present-day motion of the oceanic Nazca Plate. Our solution includes continuous GPS (cGPS) measurements at Malpelo Island offshore Colombia, two sites in the Galapagos archipelago, Easter Island and Salas y Gomez Island in the western part of the plate and Robinson Crusoe Island offshore Chile. A careful analysis of geodetic time-series reveals that (1) previous estimates using former cGPS site EISL are biased by several millimetres per year eastward due to station malfunctioning (2) north velocity component of cGPS site GLPS at Santa Cruz Island in the Galapagos is impacted by volcanic deformation at the 1–2 mm yr^{-1} level, probably caused by the recurrent volcanic activity of the Sierra Negra volcano. In addition, we find shortening at ~ 1 mm yr^{-1} between Easter Island (cGPS ISPA) and Salas y Gomez Island (cGPS ILSG), consistent with the elastic deformation induced by rapid opening at the East Pacific rise. cGPS site at Robinson Crusoe Island shows ~ 4–5 mm yr^{-1} abnormally fast East velocity induced by the visco-elastic relaxation following the Maule M_w 8.8 2010 earthquake. Using this information, we determine a new Euler pole (longitude: $-90.93°$E, latitude $56.19°$N, 0.588 deg Myr^{-1}) describing the present-day Nazca–South America Plate motion, using five sites (Malpelo Island, two sites in the Galapagos archipelago, Easter Island and Salas y Gomez Island). The proposed Euler pole provides a weighted root mean square (wrms) of residual velocities of 0.6 mm yr^{-1}, slightly higher than usually observed for other major tectonic plates and accounting for the uncertainty of potential volcanic–tectonic deformation. Our model predicts a maximum convergence rate at 65.5 ± 0.8 mm yr^{-1} at latitude $\sim 30°$S along the Chile trench, decreasing to 50.8 ± 0.7 mm yr^{-1} in northern Colombia and 64.5 ± 0.9 mm yr^{-1} in southern Chile (1σ confidence level). Comparison with the geological models NUVEL1A and MORVEL indicates constant decrease since 3.16 Ma of opening rate along the Nazca–Antarctic Plate boundary spreading centres at ~ 1 cm yr^{-1} per Myr. Combined with the ITRF2014 pole for the Pacific and Antarctic plates, our derived Euler pole predicts closure at the ~ 1 mm yr^{-1} level for Pacific–Antarctic–Nazca Plate circuit. However, combining our results with MORVEL estimates for the Cocos Plate, the non-closure of the Pacific–Cocos–Nazca Plate circuit is 9.7 ± 1.6 mm yr^{-1}, 30 per cent lower than the 14 ± 5 mm yr^{-1} reported in MORVEL model, but still significant. A small (~ 1.5 mm yr^{-1}) velocity residual at Malpelo Island neither supports the hypothesis of an independent Malpelo microplate offshore Colombia nor large scale internal deformation induced by thermal contraction. Our solution rather suggests that non-closure of the Pacific–Cocos–Nazca Plate circuit arises from the determination of the Cocos Plate motion in MORVEL, an hypothesis further supported by the large discrepancy between MORVEL's prediction and the observed GPS velocity observed at Cocos Islands (cGPS ISCO).

Key words: Plate motions; Satellite geodesy; Pacific Ocean; South America.

1 INTRODUCTION

Among the major tectonic plates, the kinematics of the oceanic Nazca Plate remains poorly understood and quantified. At geological timescales, the kinematics of the Nazca Plate has been determined from the seafloor spreading rates along its diverging boundaries with the Pacific, Antarctic and Cocos plates, together with the direction of relative motion provided by transform fault azimuths. In the MORVEL model (DeMets *et al*. 2010), the seafloor spreading rates estimated over the past 0.78 Myr are systematically slower than the estimates based on anomaly 2A averaging the motion over 3.16 Myr that was used in the NUVEL-1A model (DeMets *et al*. 1994). This result is consistent with a slowdown of the Nazca Plate of 5–6 mm yr^{-1} since 3.16 Myr, and at longer term, with a progressive slowdown of the Nazca Plate motion since at least 20 Myr (Norabuena *et al*. 1999; DeMets *et al*. 2010). However, while the Pacific–Nazca–Antarctic Plate circuit closure shows agreement with the derived kinematics and plate rigidity hypothesis, closure for the Pacific–Cocos–Nazca circuit at the Galapagos triple junction has a residual of 14 ± 5 mm yr^{-1} (95 per cent confidence level), the largest misfit found of all the plate circuits in MORVEL (DeMets *et al*. 2010), challenging the hypothesis of a single rigid Nazca Plate. Subsequently, Zhang *et al*. (2017) revised the Cocos–Nazca transform fault azimuths at four locations along the Cocos–Nazca Plate boundary and found a 3° bias clockwise with respect to the values used in MORVEL. In order to explain this small but systematic discrepancy with respect to the relative Nazca–Cocos motion predicted by MORVEL, Zhang *et al*. (2017) introduce a new microplate in the northeastern part of the Nazca Plate, referred as the Malpelo microplate (Fig. 1). However, no clear seismicity or identified active fault zone separates the hypothetized Malpelo microplate from the Nazca Plate, leading Zhang *et al*. (2017) to propose a diffuse oceanic boundary. They locate it approximately between the southern tip of the Panama transform fault and extending eastward to the trench offshore southern Colombia (Fig. 1). Nonetheless, introducing a Malpelo microplate only marginally reduces the non-closure for the 0.78 Myr Nazca–Cocos–Pacific Plate motion circuit, leaving 11–12 mm yr^{-1} to be explained.

An alternative explanation for the non-closure problem is that the Nazca Plate is not rigid and undergoes internal deformation. As the oceanic lithosphere moves away from the spreading centre, the progressive cooling should induce thermal contraction resulting in horizontal intraplate contractional strain. 1-D models suggest strain rates as large as 10^{-9} yr^{-1} for a 1-Myr-old oceanic lithosphere (Kumar & Gordon 2009), decreasing to 10^{-10} yr^{-1} for a 10-Myr-old lithosphere, a value in agreement with slight systematic deviations of the relative motion observed between right- and left-lateral transform faults (Misha & Gordon 2016). Integrated over the whole Nazca Plate which has a size of 5000×4000 km^2, such strain rates could convert into 0.5–1 mm yr^{-1} departure from a rigid motion. Although still too small to solve the Pacific–Cocos–Nazca circuit non-closure issue, thermal contraction should now be detectable from spatial geodesy as longer time-series are available.

The present-day kinematics of the Nazca Plate has been estimated using spatial geodesy. Most of the studies relied on only two sites located at Easter Island and at Santa Cruz Island in the Galapagos Archipelago (Fig. 1; Angermann *et al*. 1999; Norabuena *et al*. 1999; Sella *et al*. 2002; Vigny *et al*. 2009; Altamimi *et al*. 2012, 2017). The latest estimate from Altamimi *et al*. (2017) finds negligible residuals estimating an Euler pole using these two sites (weighted root mean square, wrms $= 0.23$ mm yr^{-1}). Fitting an Euler pole (three parameters) using only two GPS sites provides four observations to estimate three parameters, resulting in a poor control of the results. Indeed, although significant relative motion along a great circle joining the two islands would be seen in the residuals, any abnormal velocity for the component perpendicular to the great circle would not be detectable. Alternatively, GPS survey mode measurements at San Felix and Robinson Crusoe islands offshore Chile (Fig. 1), providing a better spatial sampling, were used by Angermann *et al*. (1999). Kendrick *et al*. (2003) used longer time-series and an additional campaign site in the Galapagos. They find residual velocities with respect to the best-fitting rotation pole are up to 2–3 mm yr^{-1} at most sites, but less than 0.5 mm yr^{-1} if the site at Easter Island is excluded from the calculation. In this latter case San Felix, Robinson Crusoe islands and sites on two Galapagos islands are assumed to represent the stable part of the Nazca Plate. In that view, the residual velocity of EISL site in Easter Island is 6.6 mm yr^{-1}, suggesting that Easter Island is located in a deforming zone.

Although the impact of excluding Easter Island from the Nazca Plate kinematics estimate has a minor influence on the Nazca–South America convergence rate along the margin in the northern and central Andes, it leads to differences as large as 8 mm yr^{-1} (10–15 per cent of the convergence rate) along the Chilean margin (Vigny *et al*. 2009), potentially inducing biases in interseismic models and slip budget estimates along the Chilean subduction zone.

In the present study, we use a new GPS velocity field (Fig. 1) to revisit the motion of the Nazca Plate with respect to South American Plate and discuss additional geodetic uncertainties in terms of possible tectonic and volcanic deformations. Compared to previous studies, we first benefit from longer time-series over a period of time where noise in GPS time-series has been reduced compared to the 1990s, allowing more reliable velocity estimates. Replacement of historical GPS sites, EISL at Easter Island by ISPA and GALA in the Galapagos (Santa Cruz Island) by GLPS further highlight how equipment and site change can impact velocity estimates. Two additional cGPS sites allow us to re-evaluate the ability of Easter Island and Santa Cruz Island in the Galapagos archipelago to witness the overall kinematics of the Nazca Plate. A cGPS site on Robinson Crusoe Island reveals the contribution of large scale viscoelastic relaxation from past great earthquakes at the southeastern edge of the Nazca Plate. Finally, a site on Malpelo Island offshore Colombia provides constraint on a possible independent microplate. Given the small number of available sites, each time-series is carefully analysed and we perform simple elastic models to evaluate the potential impact of several deformation processes. This study allows us to present a best selection of sites, with velocities and realistic uncertainties, and to propose new values for the Nazca–South America Euler pole.

2 GPS DATA ANALYSIS

Our data set includes observations from regional continuous stations operated by the Instituto Geofísico of Ecuador (Mothes *et al*. 2013), the Instituto Geográfico Militar of Ecuador (IGM), Servicio Geológico Colombiano (Mora-Páez *et al*. 2018), Centro Sismológico Nacional (Báez *et al*. 2018), Red Argentina de Monitoreo Satelital Continuo (Piñón *et al*. 2018), COCONet Project (UNAVCO Community 2008) and well distributed IGS stations from the global network of the International GNSS Service for Geodynamics (Johnston *et al*. 2017). In total, the final data set is composed of 57 permanent sites located on Nazca, Cocos, South America, Caribbean, Pacific and Nubia plates (Table S1).
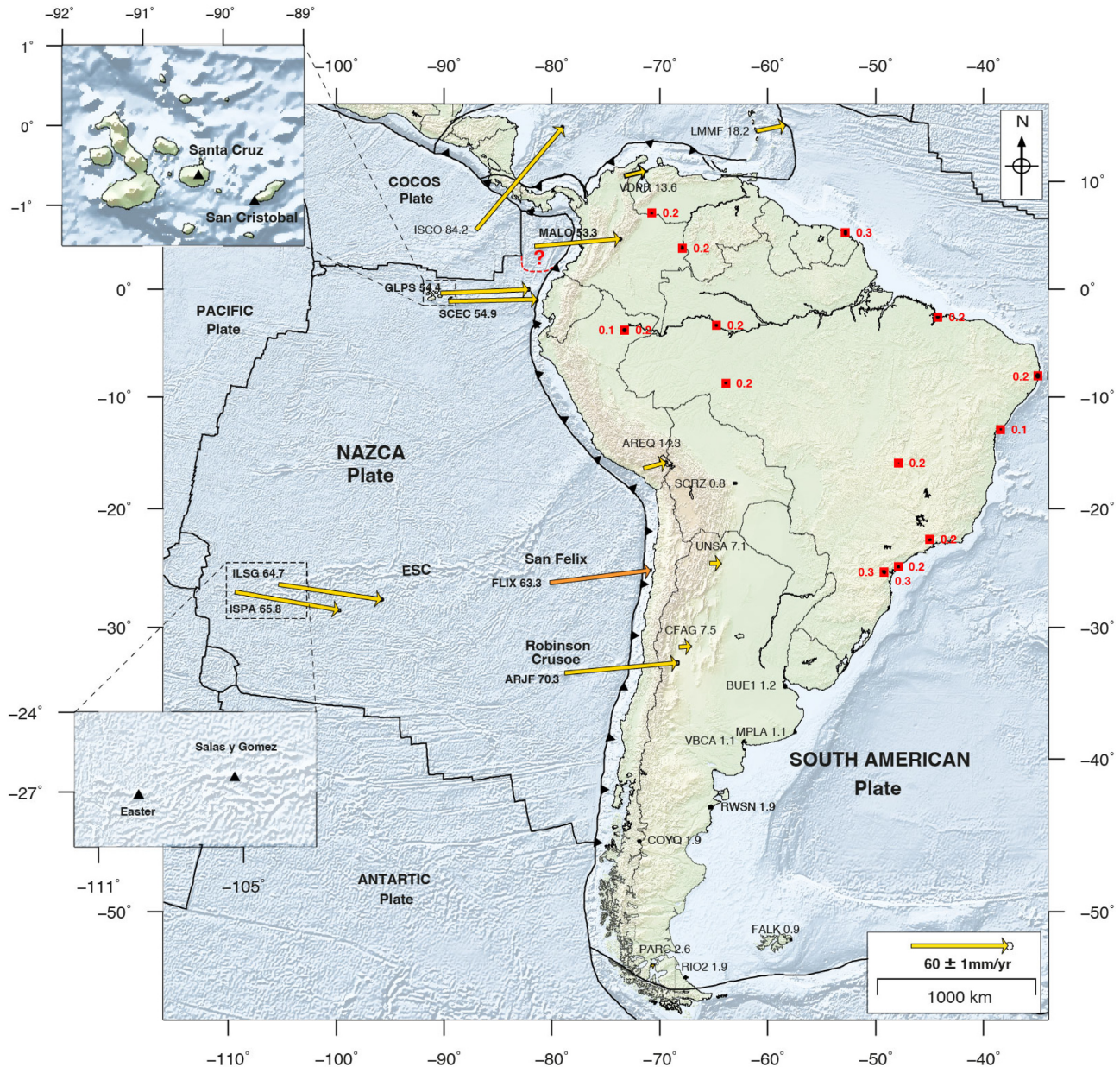
Figure 1. Map of the GPS stations used to define the stable South America (SOAM) reference frame. Red squares are sites used to compute the SOAM pole. Yellow arrows are velocities relative to SOAM reference frame. Ellipses show 95 per cent confidence. Red dashed line is the Malpelo microplate boundary proposed by Zhang *et al*. (2017). Black triangles in the inset plots show the location of GPS at Easter, Salas y Gomez, Santa Cruz and San Cristóbal islands. Orange arrow is the velocity reported by Kendrick *et al*. (2003) at the San Felix Island. ESC, Easter Seamount Chain.

Daily GPS observations were processed in sessions of 24 hr using the GAMIT/Globk software package release 10.71 (Herring *et al*. 2015, 2018) following a classical approach for geodynamics consisting in two steps. We first obtain free daily solutions by reducing double-differences of phase to coordinates. At this step, we used Earth orientation parameters provided by the IERS, and final combined orbit models from the International GNSS service for Geodynamics (IGS; Dow *et al*. 2009). We account for position variation of antenna phase centres as a function of satellite elevation and azimuth using the phase centre offsets (PCOs) and variations (PCVs) tables recommended by the IGS. Elastic response effects to ocean tides were modelled using the FES2004 model (Lyard *et al*. 2006), as well as polar and solid-earth tides following IERS/IGS (1996) standards (McCarthy 1996). We use the ionosphere-free combination to eliminate the wave delay induced by the ionosphere, and a double difference in LC phase measurements is performed to eliminate clock errors in receivers and satellites. We use the Vienna Mapping Function model (VMF1, Boehm *et al*. 2006) together with a zenithal delay every 2 hr to model the delay of the GPS signal crossing the troposphere. In the second step, we express our regional solutions with respect to the cumulative up-to-date solution from the global International GNSS Service (IGS) network (Rebischung *et al*. 2016). This IGS solution is up-to-date of the documented discontinuities and offers a parametric model

for reference sites impacted by post-seismic deformation. Daily Helmert parameters are estimated through an L1 estimator implemented in the PYACS software to produce position time-series in the ITRF2014 reference frame (Altamimi *et al.* 2017). Our solution spans the 1994–2019.9 period and includes eight sites located on the Nazca Plate: MALO (Malpelo Island), GLPS and GALA (Santa Cruz Island in Galapagos Archipelago), SCEC (San Cristóbal Island in Galapagos Archipelago), ILSG (Salas y Gomez Island), EISL and ISPA (Easter Island) and ARJF (Juan Fernandez Island; Fig. 1).

In order to ensure a reliable interpretation, we only retain time-series of positions of at least 2.5 yr of measurement to avoid bias due to seasonal variations in the secular velocity estimates (Blewitt & Lavallée 2002). Time-series of positions are then visually inspected in order to identify discontinuities or offsets caused by undocumented antenna changes, to remove remaining outliers and to exclude specific time window showing departure from a linear evolution. For sites on the South America Plate, we remove periods of non-linear post-seismic motion following large subduction earthquakes. We then simultaneously estimate velocity, annual and semi-annual terms, and offsets using the formulation proposed by Bevis & Brown (2014). For all residual time-series, spectral index of coloured noise and noise magnitude are estimated using the maximum likelihood estimator implemented in the CATS software (Williams 2008) to deduce realistic velocity uncertainties. Results show spectral indices about –1 for ∼95 per cent of the time-series evaluated, showing a combination of white noise and flicker noise as found in many studies worldwide. The velocity field in the ITRF2014 reference frame is provided in Table S1. Daily position time-series for all sites located on the Nazca Plate are shown in Figs S1–S8.

We validate our results against the velocity estimates published by the Nevada Geodetic Laboratory (Blewitt *et al.* 2018). Overall, we find non-significant differences (<0.3 mm yr^{-1}) except at ARJF, EISL, GALA and GLPS sites where differences of 0.5–1 mm yr^{-1} are due to the presence of large periods of non-linearity that we discuss in the following sections. This comparison indicates a very small influence on velocity estimates of our regional reference frame realization compared to a global network solution. We then compute a rigid rotation by minimizing the horizontal velocities from 17 sites sampling the stable part of the South American Plate (SOAM) [ARCA, ASC1, BRAZ, CHPG, CHPI, IQTS, IQUI, KOU1, NEIA, PARA, POVE, PUIN, RECF, SALU, SAVO, TEFE, UFPR] (Fig. 1 and Table S2). The weighted-root-mean-square (wrms) is 0.15 mm yr^{-1}, with a reduced chi-square of 1.1 indicating a good agreement between velocity uncertainty and the residuals. Our Euler pole in the ITRF2014 for the South America Plate is –133.28°E, 18.4°S, 0.121 deg Myr^{-1} close to the value proposed by Altamimi *et al.* (2017).

3 ANALYSIS OF POSSIBLE SOURCES OF DEFORMATION

Unlike the South America Plate where many sites provide a high redundancy and allow outliers detection, the oceanic Nazca Plate hosts only 6 different measurements locations at eight GNSS sites. In the following section, we describe a careful analysis of the velocity estimates for each site and assess the order of magnitude of potential sources of deformation before proceeding to the Euler pole calculation.
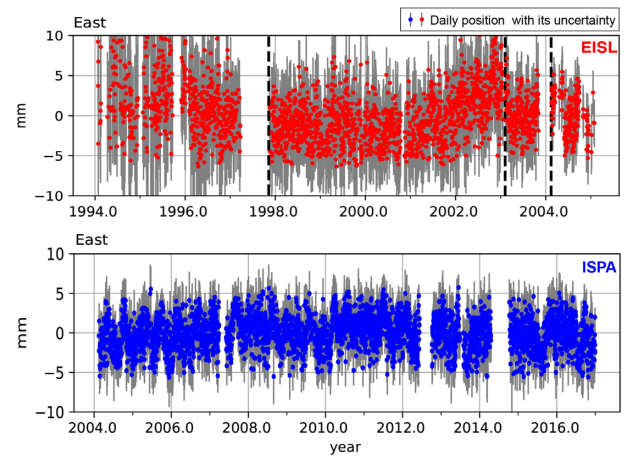

Figure 2. Residual time-series (coloured dots) for the east component of EISL and ISPA cGPS sites. Vertical dashed lines show antenna replacement dates according to the International GNSS service.

3.1 Easter and Salas y Gomez islands

3.1.1 Geodetic velocity

On Easter Island, EISL site has been operating from 1994 to 2005 and ISPA site from 2004.12 to present. The sites are separated by ∼4.0 km. Regardless of the period used to estimate the velocity, EISL and ISPA have a north velocity component which is consistent at the submillimetre per year level. In contrast, the east component of velocity appears to be dependent on the selected period. During EISL lifetime, equipment changes are documented at three dates for which offsets parameters are added to the least-squares estimate of trend. For the observation period 1994–2002.0, we find a velocity of $Ve = 66.9$ mm yr^{-1} and $Vn = -11.6$ mm yr^{-1} (norm = 67.9 mm yr^{-1}, Fig. S1) in agreement at a 1 mm yr^{-1} level with the values proposed by Kendrick *et al.* (2003) ($Ve = 67.9$, $Vn = -12.0$, norm = 69 mm yr^{-1}) using the same observation window. However, Fig. 2 also shows that the trend during the 2001–2003.1 period appears to be abnormally large compared to the trend observed during the 1994–2001 period. Velocity estimates range from 66.2 mm yr^{-1} when excluding the 2001–2003.1 period to 67.9 mm yr^{-1} when including it (Fig. S1).

ISPA benefits from ∼13 yr of continuous observations from 2004.1 to 2017 without any documented potential offset (except antenna cable replacement) nor large transients able to bias its velocity estimate during this period (Fig. 2). The estimated velocity is $Ve = 64.8$ and $Vn = -11.3$ (norm = 65.8 mm yr^{-1}, Fig. S2). This value is in agreement within the uncertainty with the lowest estimates for EISL. We checked that the dependence of the east velocity estimate on the considered period does not arise from artefact in our solution by performing the same analysis using UNR (Nevada University; Blewitt *et al.* 2018) and IGS time-series, and found a similar range of velocity estimates at EISL and ISPA.

In addition to the influence of the selected period on the estimated east velocity, we investigate the noise property of the residual time-series. For both sites, we compute the Power Spectral Density (hereinafter PSD) using the Hector package (Bos *et al.* 2013; Bos & Fernandes 2015). The obtained PSDs are similar to previous findings for global and regional cGPS networks, with a flat spectrum at high frequencies indicating white noise, and a spectra slope of roughly –1 at frequencies lower than 20 cpy (cycles per year),

consistent with flicker noise (see Fig. S1 and Table S3). No random-walk that could suggest a monument instability is detected. The PSD obtained for EISL has a power value about twice the one for ISPA, at all frequencies. Lower noise for the 2004–2017 period compared to 1994–2003 is consistent with the progressive densification of the IGS network, the improvement of satellite tracking capabilities of GPS receivers and the improvement of orbit accuracy through time (Griffiths 2019).

Aside from this improvement observed worldwide, Fig. 3 shows the daily average multipath RMS values for MP1 and MP2, data quality indicators of the raw data collected by the receiver together with the residual east time-series at EISL. The visual comparison highlights correlations between anomalous values or trend changes of MP1 and MP2 with apparent transients or increased noise in the EISL time-series. This likely suggests that the non-linear behaviour of EISL time-series arises from EISL receiver tracking problems or from changes in the environment surrounding the antenna.

This comparison suggests that previous velocity estimates for EISL might be biased at a few millimetres per year level, explaining some discrepancies among previous studies (Angermann *et al.* 1999; Kendrick *et al.* 2003; Altamimi *et al.* 2012). Therefore, the velocity estimate for ISPA is more robust and is a few millimetres per year slower than EISL velocity.

3.1.2 Possible source of deformation

Kendrick *et al.* (2003) interpret EISL velocity as being not consistent with a rigid motion defined by sites in San Felix, Robin Crusoe, and Galapagos (GALA) islands. We saw in the previous section that using the more reliable ISPA velocity explains about 50 per cent of the 6.6 mm yr^{-1} EISL residual found by Kendrick *et al.* (2003). The deformation in that part of the plate may be evaluated using the results for ILSG site, located on the Salas y Gomez Island, 400 km east of Easter Island. We first evaluate the rate of length change along a great circle joining ISPA to ILSG, a quantity which is insensitive to rotation on the sphere. We find a shortening rate of 1.1 ± 0.5 mm yr^{-1}, still significant at a 95 per cent confidence level and equivalent to 2.7 ± 1.2 nstrain yr^{-1}. This value is one order of magnitude larger than the possible effect of oceanic thermal contraction as we discussed in the introduction (Kumar & Gordon 2009). Both islands are emerged parts of the Easter Seamount Chain, a ~2500-km-long structure made of volcanic material and numerous seamounts, extending east of the East Pacific Rise, to the southern tip of the Nazca Ridge offshore southern Peru (Fig. 1). At Easter Island, the latest stage of volcanic activity was dated at 110 kyr (Vezzoli & Acocella 2009), but the most recent lava flows on Easter Island are thought to be less than 2000 yr old (Global Volcanism Program, Smithsonian Institution). While most of the Easter Seamount Chain hosts little or no seismicity, the ISC seismic reviewed catalogue from 1976 to 2018 (Engdahl *et al.* 2020) highlights an average of 2–4 earthquakes per year occurring between and around both islands (Fig. 4). A swarm of 12 shallow (<15 km depth) earthquakes occurred within 20 days in December 2000 between the two islands (~200 km from both island) where sonar images and bathymetric data have shown evidence of volcanic activity (Liu 1996; Rodrigo *et al.* 2014). Seismicity distribution therefore probably indicates several spots of more active magmatism or volcanism at the Easter Seamount Chain. The diversity of focal mechanisms (Fig. 4) indicates heterogeneous stress induced by magmatic activity rather than by a regional tectonic stress field. In the absence of additional measurements, the size and magnitude of the volcanic deformation

occurring at the Easter Seamount Chain between Easter Island and Salas y Gomez Island remains unknown. We can only comment that the large (~200 km) distance between the seismicity location and both islands most probably prevents significant volcanic deformation to bias velocity at a 1 mm yr^{-1} level at both islands. For comparison, no strain would be detected at 200 km away for the active volcano centres in the Galapagos (see Section 3.2).

As an additional attempt to understand the cause of the contractional strain rate observed between ISPA and ILSG, we evaluate the effect resulting from the far field elastic deformation induced by continuous magma injection at the fast spreading centre located ~350 km west of Easter Island. At a first glance, such a distance appears to be very large to cause a significant effect at Easter Island, but opening rates are among the fastest on Earth almost reaching 15 cm yr^{-1} (DeMets *et al.* 2010), potentially resulting in a wide area impacted at the millimetres per year level. The most similar geodynamic environment where geodetic observations are available is Iceland where the relative motion of Eurasia with respect to North America results in an opening rate of ~20 mm yr^{-1}. Geodetic results from Árnadóttir *et al.* (2009) show that contractional strain rates are observed at 100–200 km away from the spreading centres. Contractional strain rates, that is decreasing velocity magnitude with increasing distance from the spreading centre, are caused by the elastic response of the crust to the pressure induced by magma intrusion at the spreading centre. This effect can be simply modelled using vertical dislocation with tensile slip, where the depth extension of the dislocation controls the spatial extend over which significant effect will be observed at the surface. For Iceland, Árnadóttir *et al.* (2009) obtained dislocation bottom depth in the range of 5–10 km. Compared to Iceland, the fast spreading rates along the East Pacific Rise certainly results in reduced elastic thickness, both at the spreading centre and away of it as Nazca oceanic lithosphere travels faster. Elastic thickness of the lithosphere near the East Pacific Rise on the Easter and Salas y Gomez islands (along the Easter Seamount Chain) have been estimated from bathymetry and gravity data to ~2.5 ± 1 km (Liu 1996; Kruse *et al.* 1997), a value consistent with 2–3 km at the Mid-ocean ridge axis proposed by flexural studies, geological interpretations and thermomechanical models (Engeln & Stein 1984; Behn & Ito 2008; Mooney 2015).

In order to explore the potential impact of elastic deformation that would affect to the Nazca Plate velocity at ISPA and ILSG, we simulate the velocity field induced by tensile slip extending from the surface to 3 km depth using an opening rate of 140 mm yr^{-1} (DeMets *et al.* 2010). Between latitudes 22°S and 27°S, several studies identified an independent Easter microplate, embedded between the Nazca and Pacific plates, whose boundary accommodates a fraction of the Nazca–Pacific motion. Because the precise kinematics of the Easter microplate is uncertain and because our aim is to evaluate the order of magnitude of possible elastic deformation, we choose to attribute the whole Nazca–Pacific motion as the tensile slip along the Easter microplate–Nazca boundary. Results show elastic contributions of 1.1 and 0.7 mm yr^{-1} at ISPA and ILSG sites respectively, mainly impacting their east components (Fig. 5). This contribution increases to 1.4 and 0.8 mm yr^{-1} if we extend the depth of vertical dislocations to 4.0 km. For the horizontal baseline length rate of change between ISPA and ILSG, we obtain 0.4–0.6 mm yr^{-1}, a value that is consistent with the GPS results (1.1 ± 0.5 mm yr^{-1}). This calculation indicates that ISPA east velocity might be faster than the motion of the Nazca Plate at the level of 1 mm yr^{-1} and ILSG at the level of half a millimetres per year. These potential effects can be accounted for, either as additional uncertainties or as a priory correction to test their influence in the calculation of the
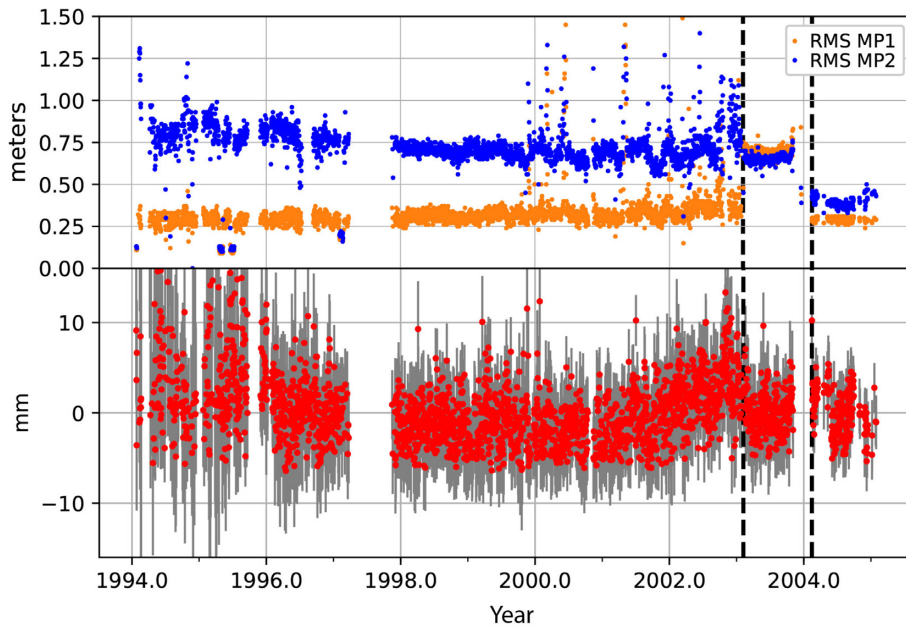
Figure 3. Comparison between Average multipath daily values (blue and orange dots) and the residual time-series from the east component of EISL site (red dots with their uncertainties). Vertical black dashed lines are the antenna replacement dates.
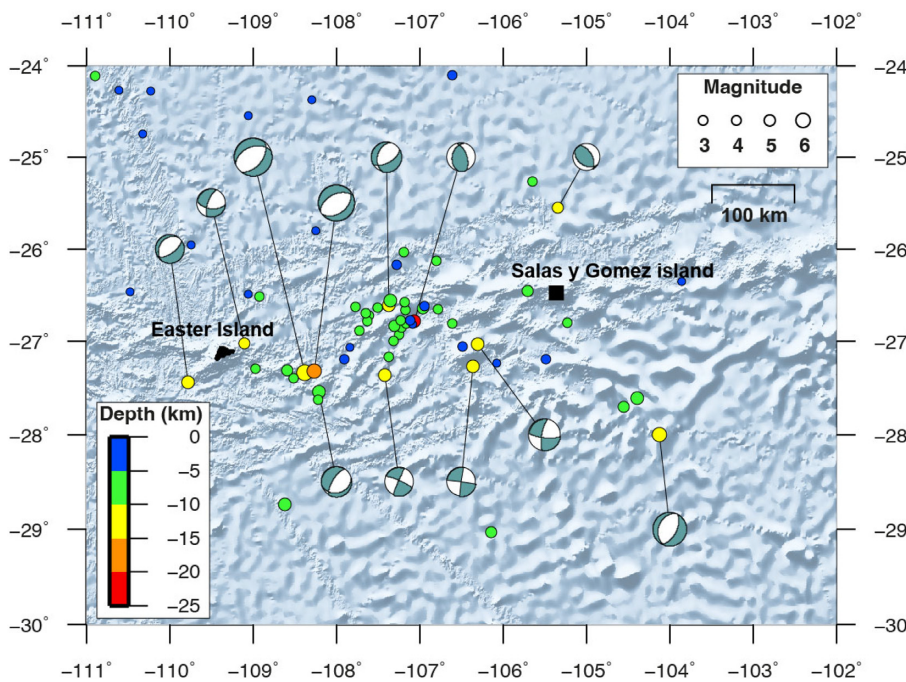

Figure 4. Intraplate seismicity in areas surrounding to the Easter and Salas y Gomez Islands. $M_b > 3.0$ earthquakes are plotted by small colour-filled circles. Earthquake reviewed catalogue is from the International Seismological Centre (ISC: Engdahl *et al.* 2020) and focal mechanism solutions are from the Global Centroid Moment Tensor (gCMT: Ekström *et al.* 2012).

Nazca Plate rotation pole. We discuss the impact of these corrections on the Nazca Euler pole estimation in Section 4.

3.2 Galapagos archipelago

Similar to Easter Island, geodetic measurements on the Galapagos archipelago have been used in all estimates of the Nazca Plate

motion. GALA site on Santa Cruz Island provided data starting in 1994, with daily data from 1996.1 to 2002.9. It has then been replaced by GLPS installed 33 m from GALA, with continuous data since 2003.0. Here, we use 4 yr of data from an additional cGPS site SCEC operated by the National Geographical Institute of Ecuador (IGM). SCEC is located on San Cristóbal Island, about 90 km east from Santa Cruz and ∼170 km away from the active
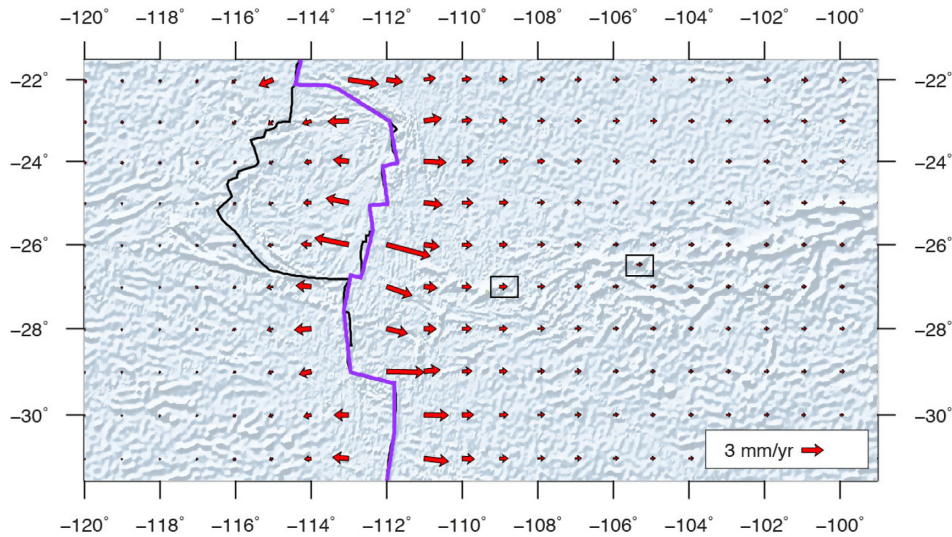
Figure 5. Elastic model at the southwestern end of the Pacific–Nazca Plate boundary. Red arrows are the predicted elastic contributions by opening rectangular dislocation elements. Unfilled black squares are the Easter and Salas y Gomez islands location.

volcanic centres. Thus, SCEC allows to evaluate potential bias in GALA and GLPS velocities induced by volcano deformation.

3.2.1 Geodetic time-series

SCEC benefits from 4 yr of observations from 2013.8 to 2017.75, with one documented offset. The velocity estimate is 54.9 mm yr^{-1} (Ve = 54.9 mm yr^{-1} and Vn = 1.3 mm yr^{-1}, Fig. S6). Fig. 6 shows the time-series at the three sites in the Galapagos, detrended using the velocity estimated for SCEC. As for EISL and ISPA, the newest site GLPS time-series shows a much lower level of noise compared to GALA. Visual inspection of the GALA time-series highlights a departure from constant linear motion with a 5–6 mm northward transient during the 1997–1998 period. It is then followed by a $\sim$2 mm yr^{-1} southward motion. Smaller changes of velocity might also exist for the 2000–2002 period on the East component. For GLPS, without any documented antenna change, a slight reversal of motion is observed around 2008 for the north component. Pre-2008 and post-2008 velocity differs by $\sim$1 mm yr^{-1} on the north component.

3.2.2 Volcanic deformation

In the Galapagos archipelago, active volcanic centres are located on Fernandina and Isabella islands, at 140 and 90 km west to southwest from GALA/GLPS and 170 and 220 km west from SCEC. During the 1994–2018 period, Fernandina volcano and Sierra Negra volcano on Isabella Island have experienced several episodes of large deformation at their calderas. Most of them ended in volcanic eruptions while for a few others high seismicity rate, degassing and ground deformation occurred without eruption (Fig. 7). Interferometric synthetic aperture radar (InSAR) and GNSS data identified large inflation and deflation processes at the Fernandina, Sierra Negra and Alcedo volcanoes, suggesting complex magmatic systems composed of one or two shallow magma reservoirs (Chadwick *et al.* 2006; Geist *et al.* 2008; Bagnardi & Amelung 2012; Baker 2012; Galetto *et al.* 2019). Although many studies have focused on

estimating the geometry and volume of these shallow magma reservoirs, their deeper portions that would induce larger scale surface deformation remain uncertain. Past and recent volcanic processes at the Fernandina-Alcedo and Sierra Negra-Cerro Azul volcanoes suggest interactions between them that could possibly be fed by a common deep magma reservoir (Baker 2012).

Deformation at Sierra Negra produced faulting on an intracaldera preexisting fault system and caldera floor uplift cumulative $\sim$5 m (between 1992 and 2005.8) prior to the October 2005 eruption. $\sim$2.7 m uplift took place between 1992 and 1999, including intracaldera faulting causing $\sim$1.2 m of slip (equivalent to a M_w 5.7 earthquake) during $\sim$1997–1998, followed by subsidence from $\sim$2000 to 2002, and then $\sim$2.3 m of uplift during the 2003–2005.8 period (Amelung *et al.* 2000; Chadwick *et al.* 2006; Geist *et al.* 2008). Eventually, several deformation phases (uplift and subsidence of the caldera floor) were recorded in all geodetic stations at Sierra Negra volcano after the 2005.8 eruption. The last one, recorded by InSAR and local cGPS measurements, reached $\sim$0.9 m of caldera floor uplift (uplift cumulative >6.5 m between 2006 and 2018) with the fastest inflation rates ($\sim$70 cm yr^{-1}) ever recorded worldwide between June 2017 and June 2018. This deformation was accompanied by intense seismicity located below 16 km depth, with additional shallow seismicity around the caldera prior to the June 2018 eruption (reports: Instituto Geofísico of Ecuador).

Fig. 6 shows several correlations between non-linear motions observed in geodetic time-series and deformation processes of Sierra Negra volcano. We note a good correlation between the inflation and deflation occurring at Sierra Negra from 1997 to 2002 (Chadwick *et al.* 2006; Geist *et al.* 2008) with variations in the north component of GALA time-series. For GLPS, the negative slope observed between the 2003 and 2006 corresponds to the 2003 and 2005.8 volcanic inflation period at Sierra Negra. Another change visible on the east component during 2017.5–2019.8 correlates with the pre-co and post-eruption period at Sierra Negra. In the meantime, despite only scarce data are available for SCEC, no change is visible during the first three months after the onset of the 2018 pre-eruptive activity, suggesting that San Cristóbal Island is located far enough to remain unimpacted by volcanic deformation.
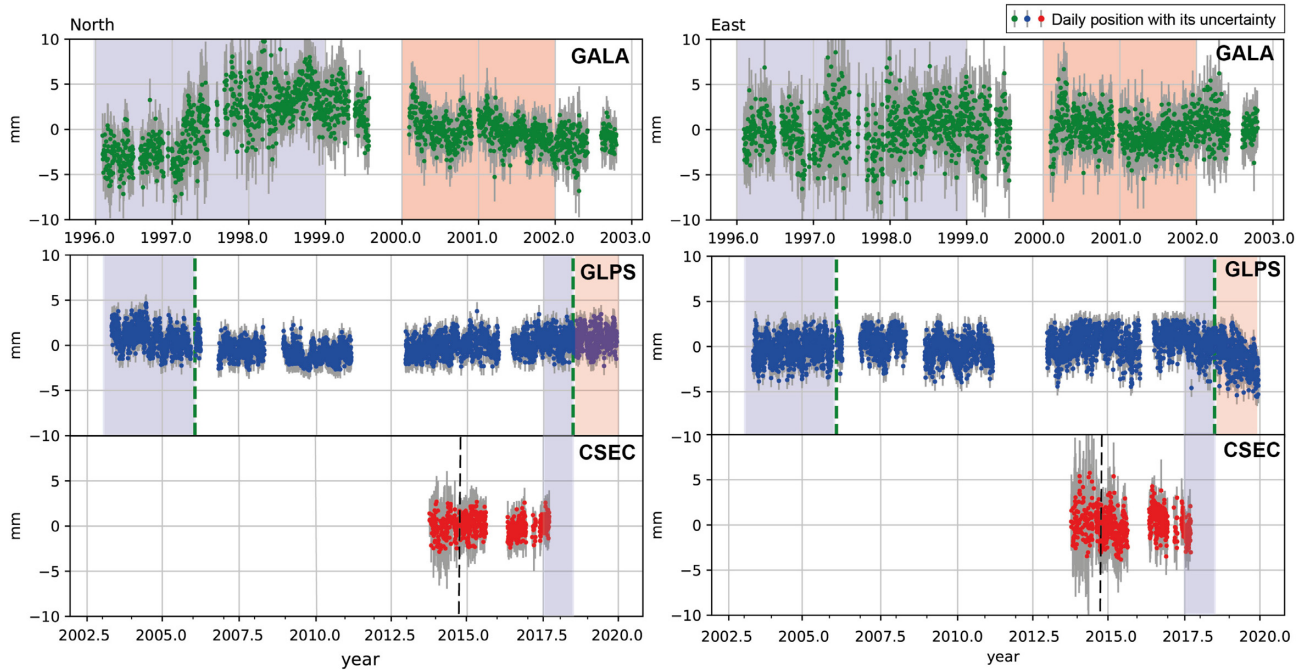
Figure 6. Daily horizontal position time-series (coloured dots) with associated uncertainty (grey bars) for GALA, GLPS and SCEC sites. The best-fitting velocity for SCEC has been removed from the raw time-series. Light pink and light blue stripes are time windows of volcanic deflation and inflation observed at Sierra Negra volcano, respectively. Green dashed lines depict the onset of Sierra Negra's eruptions in 2005.8 and 2018.7. Vertical black dashed line indicates the antenna replacement date.
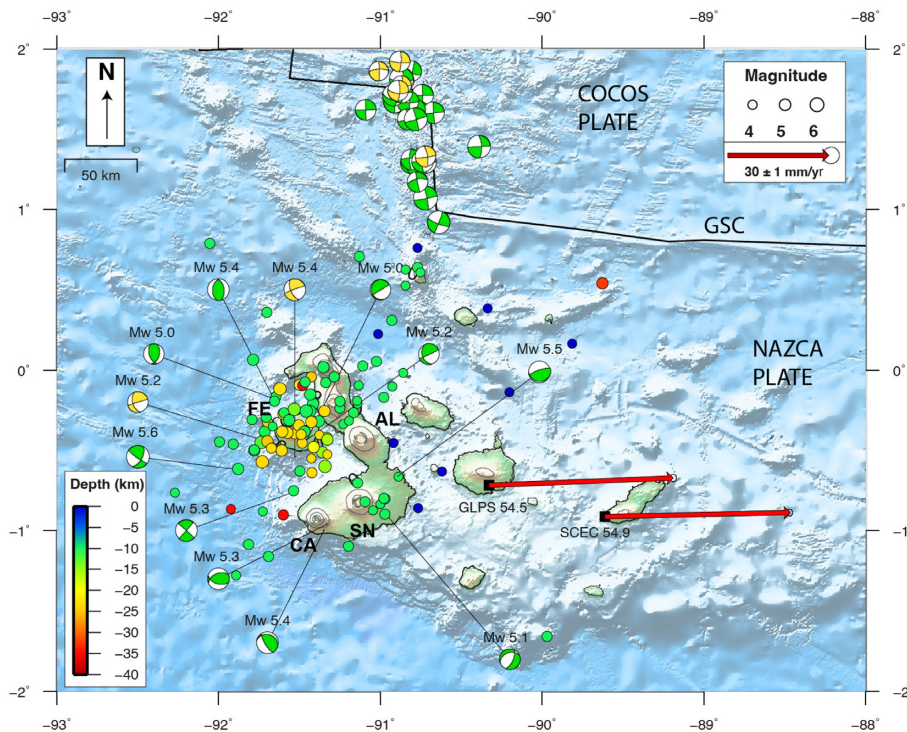

Figure 7. Seismic activity in the Galapagos Archipelago. $M_b > 4.0$ earthquake reviewed catalogue restricted to 40 km depth between 1976 and 2018 is from the International Seismological Centre (ISC: Engdahl *et al.* 2020) and $M_w \geq 4.5$ focal mechanism solutions are from the Global Centroid Moment Tensor (gCMT: Ekström *et al.* 2012). Earthquake depths and focal mechanism depths are depicted by the colour scale (bottom left). Red arrows are GPS velocities with respect to stable South America reference frame (SOAM). Velocity error ellipses are at the 95 per cent confidence level. SN, Sierra Negra; FE, Fernandina; CA, Cerro Azul and AL, Alcedo volcanoes. GSC, Galapagos Spreading Center.

Removing the deformation periods of Sierra Negra, we find a velocity estimate of $Ve = 54.4$ mm yr^{-1}, $Vn = 2.3$ mm yr^{-1} (norm = 54.5 mm yr^{-1}, Fig. S5) for the 2008.5–2017 period for GLPS. We estimate the velocity for GALA using the 1996–2003 period, but removing the 1997–1998 period during which the ∼7 mm 1997–1998 northward transient is observed and solve for an offset during this period. This procedure provides a velocity of $Ve = 55.2$ mm yr^{-1}, $Vn = 1.5$ mm yr^{-1} (55.2 mm yr^{-1}, Fig. S4) that agrees (difference is 0.7 mm yr^{-1}) with GLPS velocity estimates.

We further evaluate the consistency between GLPS and SCEC velocities. The baseline rate is 0.7 ± 0.5 mm yr^{-1}, not significant at the 95 per cent confidence level. However, the relative motion between the two sites has a significant component perpendicular to the baseline. Given the short distance (80 km) between SCEC and GLPS together with the large distance of the Nazca–South America poles (∼90–98°W, 54–61°N) from the Galapagos archipelago, we can compare the velocity change predicted by previously published Euler poles and the relative residual velocities. The velocity of GLPS with respect to SCEC expected from a rigid motion is –0.4 and –0.1 mm yr^{-1} for the east and north component, respectively. Our best estimates (removing periods of known volcanic deformation described above) is –0.3 and +1 mm yr^{-1}. This result suggests that the north component of GLPS velocity might be impacted by volcanic deformation at the 1 mm yr^{-1} level.

As for the Easter Island area, we also evaluate the possible contribution of elastic deformation associated with magma intrusion at the Nazca–Cocos Plate boundary. Between longitudes 91°W and 85°W, seafloor spreading rates along the Galapagos Spreading Center is ∼58 mm yr^{-1} (DeMets *et al*. 2010) with a magma intrusion capacity from 5 to 50 million m^3 every 500 yr (Perfit & Chadwick 1998). Both GALA/GLPS and SCEC are located 180 km from it. Using tensile dislocations from the surface down to 3 km, the model predicts ∼0.3 mm yr^{-1} southward velocity at GLPS and SCEC sites. This displacement value is within the range of the GLPS and SCEC velocity uncertainties, so we discard this contribution.

In summary, correlations between velocity changes for the cGPS sites on Santa Cruz Island and eruptions periods suggest a potential impact of volcanic deformation at the 1 mm yr^{-1} level on the north component. Using velocity estimates for SCEC, located on San Cristóbal to ∼170 km away from the active volcanic centres, provides a more reliable estimate of the Nazca Plate motion.

3.3 San Felix and Robinson Crusoe islands

3.3.1 Geodetic velocity

In the southeastern part of the Nazca Plate, velocity estimates from survey GPS measurements in distinct sites within San Felix (ISFE, FLIX) and Robinson Crusoe (IRBS, RBSN) islands published by Angermann *et al*. (1999) and Kendrick *et al*. (2003) highlight discrepancies of ∼3 mm yr^{-1} between them [FLIX = 63.3 mm yr^{-1}, RBSN = 63 mm yr^{-1} for Kendrick *et al*. (2003) versus ISFE = 60.1 mm yr^{-1} and IRCR = 66 mm yr^{-1} for Angermann *et al*. (1999)]. These differences may come from different data sets and observation spans, different reference frame (ITRF) adopted in the data analysis and will result in a different estimates of rotation pole for the Nazca–South American plates. Both studies only used two epochs of measurements, potentially leading a bias of a few millimetres per year. Since 2013.8, a new continuous GPS site (ARJF) has been installed on the Robinson Crusoe Island, but has a large data gap between 2016.5 and 2019.7. A 15 mm eastward offset is observed (see Fig. S8) at the time of the M_w 8.3 2015 September 16 megathrust Illapel earthquake located ∼700 km east–northeast of ARFJ. Pre-Illapel earthquake velocity estimated from 2 yr of measurements is 70.3 mm yr^{-1} ($Ve = 70.1$ mm yr^{-1}, $Vn = 5.0$ mm yr^{-1}) and post-Illapel estimated from 2016 to 2019.8 is 69.9 mm yr^{-1} ($Ve = 69.6$ mm yr^{-1}, $Vn = 6.6$ mm yr^{-1}), but suffers from the data gap between 2017.6 and 2019.7. Despite their uncertainty, the velocity change is consistent with the expected motion for post-seismic deformation with increased velocity towards the Illapel earthquake rupture.

3.3.2 Post-seismic deformation

During the 2013.5–2020 period, Robinson Crusoe Island has been converging towards South America at a rate 4–7 mm yr^{-1} faster than estimates obtained from surveys conducted during the 1990s. This change is significant even taking a conservative error budget for survey mode GPS measurements collected in the 1990s. Viscoelastic relaxation following the 2010 M_w 8.8 February 27 Maule great earthquake in Chile provides the most likely explanation for the observed acceleration. Robinson Crusoe Island is located 700 km offshore in front of the northern extent of the Maule earthquake rupture area (Delouis *et al*. 2010; Vigny *et al*. 2011). Previous studies have shown that the viscoelastic relaxation in the asthenosphere during the 5 yr following the 2010 M_w 8.8 Maule earthquake has induced a widespread horizontal deformation pattern extending ∼2000 km from the trench between latitudes ∼32°S and 40°S (Klein *et al*. 2016). According to viscosity values derived from several studies, several decades are required before viscorelaxation induced deformation becomes lower than 1 mm yr^{-1} level even for sites located several hundreds of kilometres from the rupture area (Khazaradze *et al*. 2002; Wang *et al*. 2007; Suito & Freymueller 2009; Klein *et al*. 2016). These results have been constrained using the GPS data only available inland on the South America continent. Although large asymmetry in the shape of the viscoelastic relaxation pattern is expected due to (1) the dip of the fault which creates asymmetry of the coseismic stress change in the asthenosphere and (2) the viscosity structure below the Andes and the South America continent (Klein *et al*. 2016) that is different below the oceanic Nazca Plate. Fig. 9 shows simple velocity estimates (without applying any correction) for the 2016–2020 period expressed with respect to stable South America, as a proxy of the ongoing post-seismic deformation 6–10 yr after the Maule earthquake. This is an approximation since locking along the subduction is neglected, but should be small at several hundred kilometers away from the trench. Interestingly, we notice that the difference of geodetic velocities pre-Maule (Kendrick *et al*. 2003) and post-Maule (this study) earthquake at Robinson Crusoe has the same order of magnitude (∼5 mm yr^{-1}) as the velocity for onshore sites located at equivalent distance from the Maule rupture area (Fig. 9).

The observed large impact of the Maule earthquake on the velocity at Robinson Crusoe Island raises the question of the possible impact of even greater megathrust earthquakes along the Chilean subduction on pre-Maule velocities. Indeed, the northern extent of the Valdivia M_w 9.5 1960 rupture is thought to abut against the southern part of the Maule earthquake rupture area, being only 10 per cent further away (750 km) from Robinson Crusoe Island than the Maule earthquake. Influence of the viscoelastic relaxation
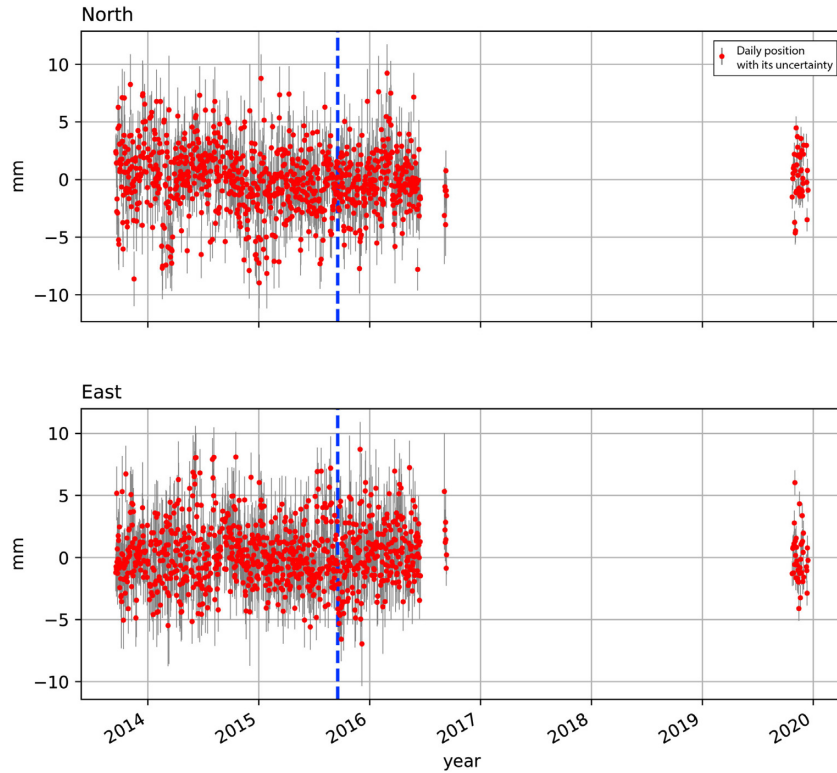
Figure 8. Daily position time-series at the ARJF site (Robinson Crusoe Island) after applied linear regression using least square. Vertical blue dashed lines show the date of M_w 8.3 Illapel earthquake.
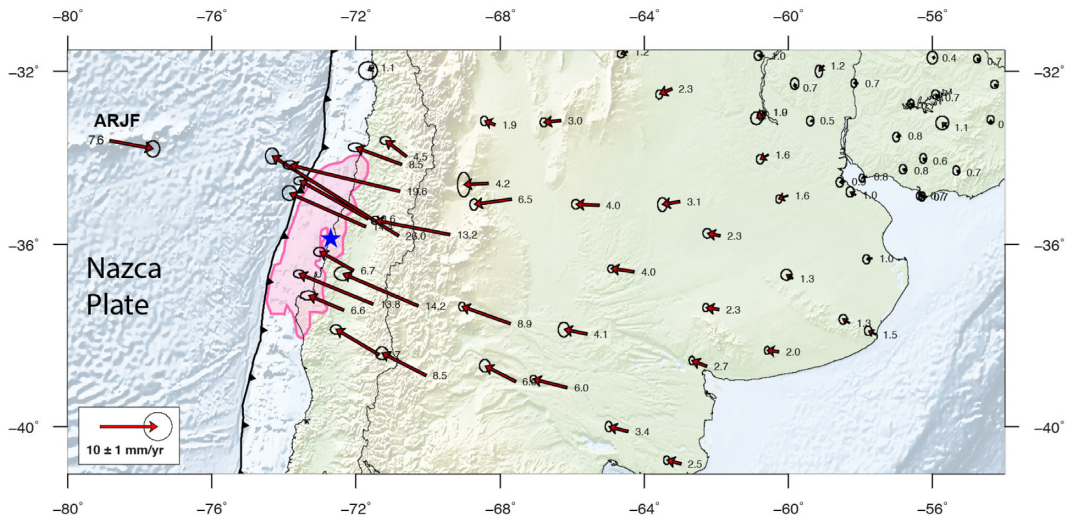

Figure 9. Maule earthquake post-seismic velocity estimated during the 2016–2020 period. Blue star is the epicentre of the 2010 Maule earthquake. Pink area is the 4 m iso-contour of coseismic slip distribution from Vigny *et al.* (2011). The velocity reported for the Robinson Crusoe Island at ARJF is the difference between the pre-Maule earthquake velocity estimated by Kendrick *et al.* (2003) and our post-Maule earthquake estimate.

has been documented for 40 yr following the earthquake (Khazaradze *et al.* 2002; Wang *et al.* 2007). Thus, some influence on the 1990s derived velocity cannot be ruled out. In conclusion, because ARJF is likely impacted by post-seismic deformation, ARJF data cannot be used to constrain the Nazca Plate motion. In addition, pre-Maule velocities at Robinson Crusoe Island (RBSN and IRCR, Angermann *et al.* 1999; Kendrick *et al.* 2003) are also suspected to be biased by the post-seismic deformation induced by the Valdivia 1960 mega-earthquake.

3.4 Malpelo island

3.4.1 Geodetic velocity

Malpelo Island is located offshore Colombia at the northeastern tip of the Nazca Plate (Fig. 10). This part of the Nazca Plate is squeezed between the Panama transform fault, active spreading centres north of the Galapagos Archipelago, the boundary with the proposed Coiba microplate (Lonsdale & Klitgord 1978; Pennington 1981;
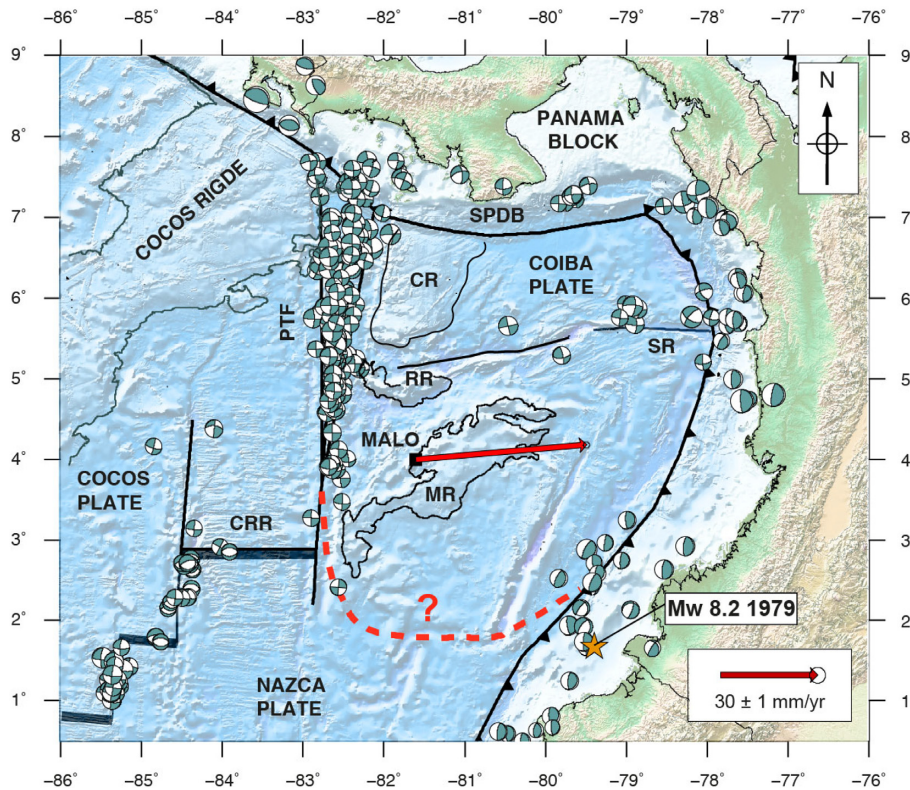
Figure 10. Seismo-tectonic map of the northeastern part of the Nazca Plate. CR, Coiba Ridge; MR, Malpelo Ridge; RR, Regina Ridge; PTF, Panama Transform Fault; SPDB, South Panama Deformed Belt; CRR, Costa Rica rift; SR, Sandra ridge [After Pennington (1981), Lonsdale (2005) and Adamek *et al.* (1988)]. The red arrow is the GPS velocity for MALO (Malpelo Island) with respect to South America. Focal mechanism solutions (light green beach balls) for $M_w > 4.5$ are from the Global Centroid Moment Tensor (gCMT: Ekström *et al.* 2012) from 1976 to 2018 restricted to 40 km depth. Red dashed line is the Malpelo–NAZCA Plate boundary proposed by Zhang *et al.* (2017). The orange star is the epicentre of the 1979 M_w 8.2 Tumaco earthquake (Kanamori & McNally 1982).

Adamek *et al.* 1988) to the north and the subduction zone. We do not find any impact from the 2016 M_w 7.8 Pedernales earthquake (Nocquet *et al.* 2016) that ruptured a 110-km-long segment of the subduction, ∼400 km southeast of Malpelo island (Fig. S7).

3.4.2 Possible sources of deformation

We assess possible elastic contributions to the velocity at Malpelo Island using the prediction from a regional kinematic elastic block model (Mccaffrey 2002; Meade & Hager 2005; Meade 2007). Our model includes the Panama Transform Fault separating the Nazca Plate from the Cocos Plate, modelled as a vertical rectangular dislocation. The locking depth is fixed to 13 km based on the average of hypocentres depth provided by the ISC-GEM global instrumental earthquake catalogue (version 7.0; Di Giacomo *et al.* 2015). As before, we model the elastic effect from the spreading centres northeast of the Galapagos using tensile dislocation from the surface down to 3 km depth. Large megathrust earthquakes occur in Colombia and Ecuador (Kanamori & McNally 1982; Nocquet *et al.* 2016), as a result of significant locking along the subduction interface. We model the interseismic effect using a uniform coupling of 80 per cent down to a depth of 50 km, consistently with the results of previous studies (Trenkamp *et al.* 2002; Nocquet *et al.* 2014; Mora-Páez *et al.* 2019). We impose the Euler Pole for the Cocos Plate from the MORVEL model (DeMets *et al.* 2010), from the ITRF2014 model for the Nazca Plate (Altamimi *et al.* 2017) and for Panama block from the model of Kobayashi *et al.* (2014). The subduction separates the subducting Nazca Plate from

the North Andean Sliver (NAS), a continental domain moving with respect to South America at ∼1 cm yr^{-1} (Pennington 1981). We model the NAS motion using the Euler pole proposed by Nocquet *et al.* (2014).

Fig. 11 shows the predictions of our forward model. The dominant elastic contribution comes from the Panama Transform fault located ∼110 km west of Malpelo Island, where elastic effect of right-lateral Nazca–Cocos Plate motion at ∼66 mm yr^{-1} (Fig. 11b) induces 1.3 mm yr^{-1} mainly at the north component at Malpelo Island. This amount reduces to 1.1 mm yr^{-1} taking a locking depth of 10 km for the vertical fault (Panama Transform fault). Elastic contribution induced by locking at the subduction interface is 0.7 mm yr^{-1} pointing out N–NW at the Malpelo site, hence reducing the effect from the Panama Transform Fault.

Adamek *et al.* (1988) suggest the existence of a Coiba microplate, squeezed between the northeastern edge of the Nazca Plate and the Panama Block. North of Malpelo Island, an east–west trending shear zone seems to coincide with the Sandra ridge, which is proposed as the Coiba–Nazca Plate boundary (Lonsdale & Klitgord 1978; Adamek *et al.* 1988; Marcailloud *et al.* 2006). This plate boundary has been classified as active since ∼1 Myr and seismicity is regularly recorded from global network (Fig. 10). Regional seismotectonic analyses conclude that if this microplate exists, its southern boundary would accommodate a small fraction of the relative motion between Nazca Plate and Panama block (Adamek *et al.* 1988). In order to assess possible influences from the Coiba microplate in the regional kinematics and subsequently at the Malpelo velocity, we perform a second block model including the Coiba
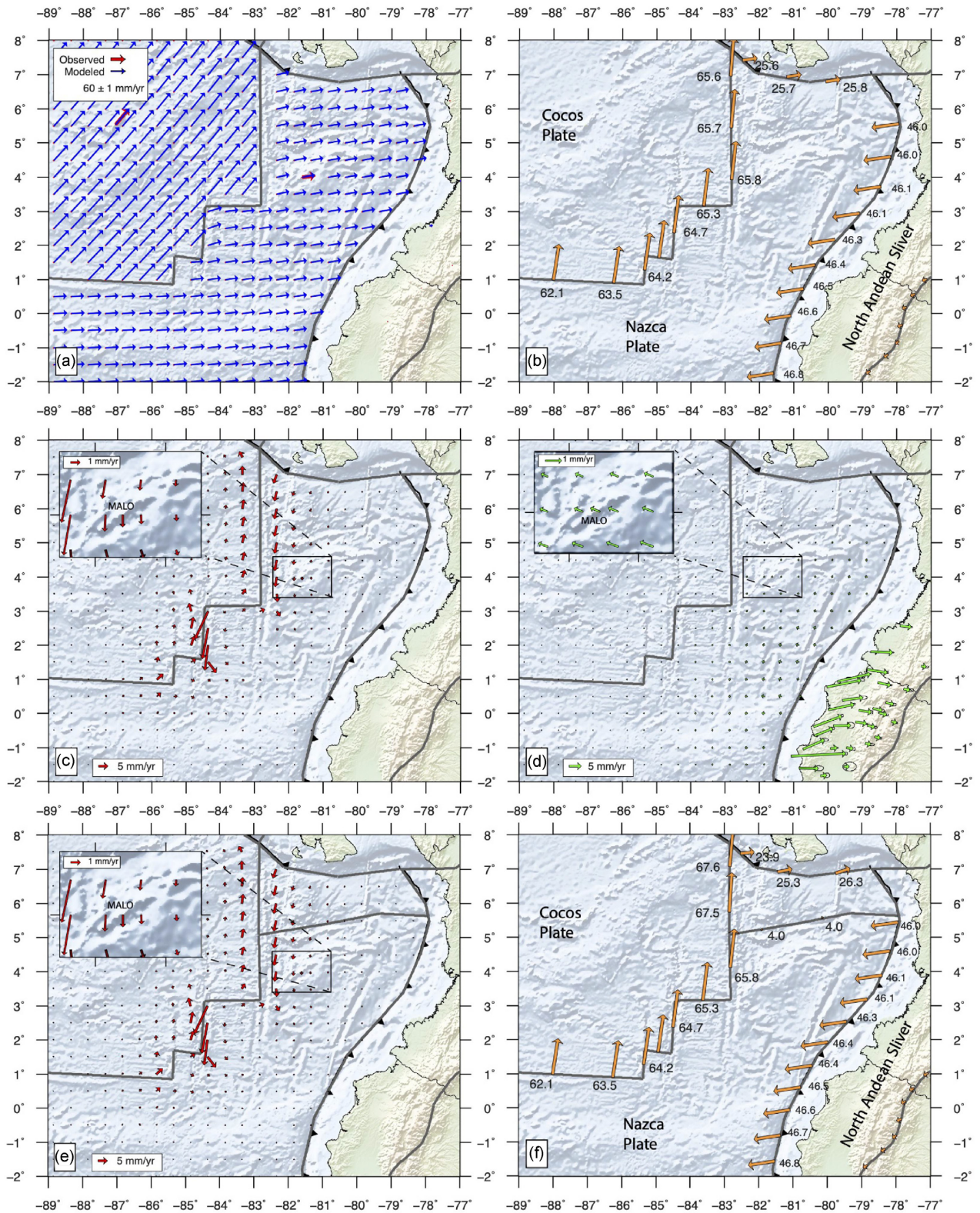
Figure 11. Forward Elastic Block model results for the northern part of the Nazca Plate. (a) Observed (red arrows) and predicted (blue arrow) velocities with respect to South America. (b) Plate motion at the Nazca Plate boundaries. Values are in mm yr^{-1}. All arrows are with respect to the Nazca Plate. (c) Predicted elastic contribution from the Nazca–Cocos Plate boundaries. (d) Elastic contribution from the Nazca–North Andean Sliver subduction zone. (e) Same as Fig. (c) but including the Coiba microplate. (f) Same as (b) but including a priory slip of 4 mm yr^{-1} at the Coiba–Nazca Plate boundary.

Table 1. GPS velocities with respect to South America for sites located on the Nazca Plate. Longitude and latitude in decimal degrees. Ts, time span of GPS observations used in the velocity estimate. σVe and σVn are the east and north velocity uncertainties derived from the noise analysis.

Site	Longitude (°)	Latitude (°)	Ve (mm yr^{-1})	Vn (mm yr^{-1})	σVe	σVn	Ts (yr)	WRMS Ve (mm)	WMRS Vn (mm)
ARJF	−78.833	−33.629	70.0	6.4	0.48	0.57	2013.7–2019.9	3.2	2.7
EISL	−109.383	−27.148	66.0	−12.1	0.51	0.37	1996–2004	6.0	1.9
FLIX[a]	−80.088	−26.297	62.8	7.7	0.2	0.2	∼1994, 2001		
GALA	−90.304	−0.742	55.2	1.5	0.53	0.45	1996–2002.5	1.7	2.0
GLPS	−90.304	−0.743	54.4	2.3	0.40	0.31	2008.5–2017	1.6	1.0
ILSG	-105.362	−26.473	64.0	−9.5	0.51	0.41	2012.9–2017.9	2.9	2.5
ISPA	−109.344	−27.125	64.8	−11.3	0.28	0.38	2004.1–2017	2.0	3.0
MALO	−81.606	4.003	53.1	4.6	0.39	0.40	2010.5–2015.9	1.8	2.1
RBSN[a]	−78.840	−33.630	62.5	7.8	0.40	0.60	∼1994, 2001		
SCEC	−89.615	−0.903	54.9	1.3	0.32	0.42	2013.8–2017.8	2.3	1.4

[a]Velocities reported by Kendrick *et al.* (2003) from 2 survey GPS measurements.

microplate and assigning left-lateral strike slip rate at the Coiba–NAZCA boundary from 1 to 8 mm yr^{-1} by steps of 1 mm yr^{-1}. The upper value of 8 mm yr^{-1} is constrained by the fact that the slip rate at the South Panama Deformed Belt must be similar to the motion of ∼22 mm yr^{-1} observed at several cGPS in Panama (Table S1 and Mora-Páez *et al.* 2019). All models indicate a negligible (∼0.1 mm yr^{-1}) contribution of this plate boundary to the velocity at Malpelo Island (Figs 11f and e).

The subduction segment along northern Ecuador and southern Colombia experienced a series of five megathrust earthquakes with $M_{\rm w} \geq 7.7$ that started with the $M_{\rm w}$ 8.6–8.8 1906 earthquake, which broke a ∼500-km-long segment of the megathrust (Kanamori & McNally 1982; Nocquet *et al.* 2016; Ye *et al.* 2016). In northern Ecuador and southern Colombia, the last documented earthquake is the 1979 $M_{\rm w}$ 8.2 (Tumaco earthquake, Fig. 10). Based on simple viscoeleastic models, White *et al.* (2003) and Mora-Páez *et al.* (2019) suggested the effect of postseismic deformation following the 1979 earthquake has decayed from ∼3 mm yr^{-1} in the 1990s to 0.5–1 mm yr^{-1} (from 2009 to 2019) on inland sites located at latitude 2.5°N, located ∼300 km away from the the 1979 $M_{\rm w}$ 8.2 earthquake rupture area. Malpelo Island is located ∼300 km northwest of the 1979 rupture area. Contributions from the viscoelastic relaxation processes in the asthenosphere is expected to be small, but would induce southeastward motion for MALO.

In summary, we find ∼1.0 mm yr^{-1} of possible elastic contribution to the Malpelo velocity from the Cocos–Nazca and Nazca–NAS relative motions and a negligible influence of Coiba microplate.

4 NAZCA–SOUTH AMERICA EULER POLE

Based on the results of the previous section, we consider three strategies for calculating the Nazca–South America Euler pole. The first strategy considers that deformation models are speculative and might introduce bias in the Euler pole calculation. In this case, only geodetically derived velocities and associated uncertainties are used. The second strategy considers that previous models, although possibly incorrect, can still be used to add reasonable uncertainties to the geodetically observed velocities. Geodetically derived velocities are used, but uncertainties based on the deformation analysis described above are quadratically added to the geodetic uncertainty. The last strategy considers that previous models, although inaccurate at the submillimetre per year level, can still be useful to correct the largest bias and will improve the determination of the Euler

pole. We follow the three strategies and evaluate their impact on the determined Euler pole for the Nazca Plate.

In the following, we evaluate the quality of the Euler pole inversion using the weighted-root-mean-square (WRMS) of residuals and σ_0. The WRMS is defined by:

$$\text{WRMS} = \sqrt{\frac{\sum_{i=1}^{n} \left(\frac{r_{e_i}^2}{\sigma_{e_i}^2} + \frac{r_{n_i}^2}{\sigma_{n_i}^2} \right)}{\sum_{i=1}^{n} \left(\frac{1}{\sigma_{e_i}^2} + \frac{1}{\sigma_{n_i}^2} \right)}}. \quad (1)$$

Both global and regional tectonic plate kinematics studies show that WRMS is of the order of 0.2–0.5 mm yr^{-1} for tectonic plates (e.g. Altamimi *et al.* 2017; Nocquet 2012), as found for South America (0.15 mm yr^{-1}, Table S2).

σ_0, called reduced chi-square or posterior variance factor is defined by:

$$\sigma_0 = R^T C_d^{-1} R / (2n - 3), \quad (2)$$

where R is the vector of residuals, C_d^{-1} is the data variance–covariance matrix and n is the number of GPS sites included in the calculation. σ_0 quantifies the overall agreement between the obtained residuals and the uncertainty associated to the data. A value of σ_0 close to one indicates agreement between the rigid plate hypothesis and the observed residuals given the data uncertainty. A value significantly larger than 1 indicates either some plate internal deformation larger than the velocity uncertainty, or underestimated uncertainties in the data or a combination of both (Nocquet *et al.* 2001). Proper handling of velocity uncertainties usually leads to σ_0 close to 1 for most plates (e.g. Sella *et al.* 2002; Prawirodirdjo & Bock 2004). For instance, here we find $\sigma_0 = 1.1$ for the South America pole.

4.1 Euler pole from geodesy only

Here we use the subset of the best determined sites [ISPA, ILSG, GLPS, SCEC, MALO] to estimate the Euler pole. The associated velocity uncertainties are the one reported in the Table 1 derived from the time-series noise analysis.

This first calculation provides an Euler pole at (NZROT50: lon. −91.57°E, lat. 56.25°N, ω = 0.591 deg Myr^{-1}). While similar to Kendrick *et al.* (2003) (−94.4°E, 61.0°N, 0.57 deg Myr^{-1}), it predicts up to 3.5 mm yr^{-1} faster convergence rate in Chile. The WRMS for this calculation is 0.90 mm yr^{-1}. This result is already good, indicating an overall agreement at the order of 1 mm yr^{-1} between the areas sampled by the GPS data. In detail, this number is about twice

the usual value reported for most tectonic plates (e.g. Altamimi *et al.* 2017). A σ_0 of 2.9 also suggests either a non-perfect rigidity or underestimated uncertainties by a factor ∼3. The largest residuals are found for Malpelo Island (2 mm yr^{-1} southeastwards) and the north component of GLPS (1.5 mm yr^{-1} northwards).

Removing GLPS from the calculation provides a pole at (NZROT40: lon. –90.41°E, lat. 57.01°N, ω = 0.590 deg Myr^{-1}), but with lower residuals (wrms = 0.60 mm yr^{-1}) and σ_0 =2.0. Although not perfect, this calculation offers the advantage of a good sampling of the plate with sites in Easter Island, Salas y Gomez, the Galapagos and Malpelo, reasonable statistics with all residuals are below 1 mm yr^{-1}. As detailed previously, there are several reasons to consider GLPS as an outlier: the analysis of GLPS time-series described in Section 3.2 shows that the north component might be biased by ∼1 mm yr^{-1} and departs from SCEC certainly less impacted by volcano deformation and which agrees with the others sites. The impact of removing GLPS on the Nazca–South America convergence prediction is small (<0.3 mm yr^{-1}) compared to including all sites.

As an alternative, we remove MALO from the previous calculation. The obtained pole is located at (NZROT30: lon. –91.41°E, lat. 55.30°N, ω = 0.593), with wrms = 0.33 mm yr^{-1} and σ_0 = 1.3. However, the degrees of freedom is only 3, making the statics indicators less significant. In that case, MALO has a residual of 2.3 mm yr^{-1} towards southeast.

Now keeping MALO and considering both Galapagos sites as outliers, we find a pole at (NZROT31: lon. –89.67°E, lat. 58.23°N and ω = 0.59 deg Myr^{-1}), and wrms = 0.35 mm yr^{-1}, σ_0 =1.3. In that calculation, SCEC has residuals of 1.9 mm yr^{-1} mainly northward.

So small residuals, similar to the ones obtained for the major tectonic plates are obtained by considering either Galapagos sites or Malpelo as outliers. The lack of redundancy prevents us from deciding which sites from Galapagos or Malpelo might be the outlier.

4.2 Tectonic and volcanic deformation as additional uncertainties

The analysis presented in Section 3 provides some first-order information for the magnitude and direction of tectonic–volcanic deformation, which contributes to adding noise to the GPS velocities in their ability to represent the rigid motion of the Nazca Plate. In order to account for this effect, here, we simply add a variance based on our forward models to the variance estimated from our geodetic noise analysis.

In Section 3.1, we find a possible bias of 1.1 and 0.7 mm yr^{-1} on the East component of velocity for ISPA and ILSG induced by magma injection at the spreading centre delimiting the Nazca–Pacific Plate boundary. We therefore add this amount as additional uncertainty on the velocity East component now becoming 1.13 ($\sqrt{0.28^2 + 1.1^2}$) for ISPA and 0.87 ($\sqrt{0.51^2 + 0.7^2}$) for ILSG.

We saw in Section 3.2 that GLPS north component is likely biased by ∼1 mm yr^{-1}. We therefore add an uncertainty of 1.25 mm yr^{-1} to GLPS north velocity (now becoming 1.29 mm yr^{-1}). Because the active volcano centres are located west to northwest of GLPS and SCEC, we add another 0.5 mm yr^{-1} on the East component of GLPS and both component of SCEC.

Finally, MALO is potential impacted by (1) elastic effect of the Panama transform fault and (2) the earthquake cycle along the subduction located ∼300 km. The latter has two opposite effects, one being the elastic effect induced by locking along the megathrust, the other being the viscoelastic relaxation coming from past large

earthquakes, the closest being the M_w 8.2 1979 southern Colombia earthquake. Interestingly, for all Euler pole calculation, MALO residual velocity has near constant direction of N140°E, pointing towards northernmost Ecuador–southern Colombia where the M_w 8.2 1979 earthquake broke a 230 km long segment of the megathrust (Kanamori & McNally 1982). Based on this, we choose to add a 1 mm yr^{-1} uncertainty on both north and east component.

This approach provides an Euler pole at (NZROT51: lon. –90.93°E, lat. 56.19°N, ω = 0.588 deg Myr^{-1}), with wrms = 0.57 mm yr^{-1} and σ_0 = 1.1, suggesting that the uncertainties added to the geodetic noise are appropriate. This approach offers the advantage of providing better estimates of uncertainty of the Nazca kinematics and hence better reflect the uncertainty of the convergence rate along the South America subduction zone.

4.3 Tectonic and volcanic deformation as *a priori* correction to data

As a last test, we use the analysis described in Section 3 to correct the geodetic velocity from tectonic–volcanic deformation. We further make the assumption that these models are correct at the 0.5 mm yr^{-1}, quadratically added to the geodetic uncertainties.

ISPA east velocity is reduced from 64.8 ± 0.3 to 63.7 ± 0.6 mm yr^{-1} and ILSG from 64.0 ± 0.5 to 63.3 ± 0.7 mm yr^{-1} to account for elastic strain from the opening at the East Pacific Rise. GLPS is corrected from 2.3 ± 0.3 to 1.0 ± 0.6 mm yr^{-1}. SCEC is not changed but 0.5 mm yr^{-1} is quadratically added to the geodetic uncertainties. MALO is corrected from –1.5 mm yr^{-1} motion in the north N120°E to account for possible viscoelastic following the M_w 8.2 1979 Colombia earthquake, here with a 1 mm yr^{-1} uncertainty.

Using this procedure, the Euler pole found is (NZROT52: lon. –90.80°E, lat. 56.48°N, ω = 0.583 deg Myr^{-1}). The wrms is 0.39 mm yr^{-1} now similar to other plates and σ_0 = 0.8 suggesting that the 0.5 mm yr^{-1} of additional uncertainty was pessimistic.

We acknowledge that this procedure is speculative, but at least it illustrates that the sense of the velocity residuals noted in the purely geodetic calculations is in agreement with the direction and magnitude of known tectonic processes.

5 DISCUSSION

5.1 Preferred pole

The three approaches described in Section 4 lead to six different estimates for the Nazca–South America Euler pole (Table 2). We first evaluate how they differ by calculating their predicted values at different locations of the Nazca Plate boundary. For each of the six Euler poles described in the previous section, Fig. 12 shows the predicted motion for the Nazca Plate with respect to the adjacent plate. For the Antarctic and Pacific plates, we use the ITRF2014 plate model from Altamimi *et al.* (2017) and the MORVEL Euler pole for the Cocos Plate (DeMets *et al.* 2010). We calculate the velocity uncertainty by propagating the plate rotation variance–covariance matrix to the location of the model prediction, using the eq. (B1) in the Supporting information. The plate rotation variance–covariance matrix were first rescaled by σ_0, except for the model obtained using *a priori* tectonic corrections, which had σ_0 < 1.

Fig. 12 first shows that the maximum difference among the different model predictions is 1.5 mm yr^{-1} at the 95 per cent confidence level. Fig. 12 also indicates that the NZROT51 pole, derived using all the geodetic data but accounting for tectonic–volcanic uncertainty,

Table 2. Summary of Nazca–South America Euler pole estimates using different subset of sites. σ_0, posterior variance factor. First number at the solution names is the number of sites used in the Euler pole estimate.

Solution	Lon. (°E)	Lat. (°N)	ω (deg Myr^{-1})	χ^2	σ_0	WRMS (mm yr^{-1})	Associated error ellipse			$\sigma\omega$
							Semi-major	Semi-minor	Azimuth	
NZROT30	–91.41	55.30	0.593	4.9	1.3	0.33	0.66	0.20	–41.0	0.003
NZROT31	–89.67	58.23	0.590	5.1	1.3	0.35	0.60	0.20	–36.3	0.002
NZROT40	–90.41	57.01	0.590	20.9	2.0	0.60	0.50	0.18	–24.2	0.002
NZROT50	–91.57	56.25	0.591	60.8	2.9	0.90	0.46	0.15	–11.1	0.002
NZROT51	**–90.93**	**56.19**	**0.588**	8.1	1.1	0.57	0.96	0.22	–53.3	0.006
NZROT52	–90.80	56.48	0.583	5.0	0.8	0.39	0.73	0.20	–38.8	0.004

Table 3. Summary of predicted convergence velocities at the A, B and C locations (Nazca–SOAM Plate boundary) depicted in Fig. 12. A (lon: –80.95°, lat: 0.28°), B (lon: –78.78°, lat: -12.38°) and C (lon: –72.57°, lat: –31.0°) are selected site coordinates along the trench axis. Predicted velocities are computed from the previous and current Nazca–SOAM poles. NS, number of geodetic sites used (∗ corresponds to solutions derived from geological data). Vel, velocity magnitude in mm yr^{-1} and Az, azimuths in degrees.

Solution	Lon (°E)	Lat (°N)	Rate (deg Myr^{-1})	NS	Predicted velocities					
					A		B		C	
					Vel	Az	Vel	Az	Vel	Az
DeMets *et al.* (1994)	–94.0	56.0	0.72	∗	67.0	81.3	75.1	81.0	80.1	78.2
Larson *et al.* (1997)	–95.2	43.8	0.74	2	58.6	75.6	69.9	76.1	80.3	73.5
Norabuena *et al.* (1999)	–93.7	47.4	0.624	2	52.0	78.5	60.8	78.5	68.5	75.7
Angermann *et al.* (1999)	–91.7	48.8	0.59	4	49.9	80.7	58.1	80.4	64.9	77.4
Sella *et al.* (2002)	–91.18	52.13	0.633	2	55.9	82.1	64.0	81.7	70.1	78.7
Kendrick *et al.* (2003)	–94.39	61.01	0.569	3	55.7	82.6	61.0	82.2	63.2	79.6
Vigny *et al.* (2009)	–95.20	55.90	0.61	2	56.8	80.5	63.6	80.3	67.8	77.5
DeMets *et al.* (2010)	–98.0	54.9	0.666	∗	61.7	78.3	69.3	78.3	74.1	75.7
Altamimi *et al.* (2012)	–94.01	55.06	0.603	2	55.5	81.0	62.5	80.7	67.0	77.9
Altamimi *et al.* (2017)	–92.9	54.78	0.599	2	54.9	81.7	61.9	81.3	66.6	78.4
This study (NZROT51)	–90.93	56.19	0.588	5	54.6	83.4	61.2	82.8	65.4	79.9

provides an average value of all Nazca Euler pole predictions. Furthermore, its 95 per cent level confidence region encompasses all the other Euler pole predictions, except NZROT40 and NZROT31, whose predictions would fall inside the 97 per cent confidence level region. Therefore, we propose the NZROT51 solution as our preferred Euler pole and associated uncertainty to describe the current Nazca Plate motion.

As a second evaluation, we test the level of agreement between our preferred pole (NZROT51) and previously published poles (summarized in Table 3) in terms of predicted Nazca–SOAM convergence velocities at the A, B and C site locations displayed in Fig. 12. Overall, Table 3 first shows that predicted velocities derived from previous geodetic Euler poles differ by ∼1 cm yr^{-1} at the Ecuadorian (Northern Andes) and Peruvian (Central Andes) trench and by ∼1.5 cm yr^{-1} at the Chilean trench (Fig. 13). For all sites, the Euler pole from Larson *et al.* (1997) predicts faster velocities than the other geodetic poles (Fig. 13a). As found in previous geodetic studies, convergence rates from the geological models Nuvel1A (DeMets *et al.* 1994) and Morvel (DeMets *et al.* 2010) are faster than those predicted by the geodetic poles for all site locations (except for Larson *et al.* 1997; Fig. 13a).

Excluding Larson *et al.* (1997), we find that the prediction of our pole falls close to the average of previous geodetic studies. At site A (lon. –80.95° and lat. 0.28: Ecuador–Colombia trench), the average prediction is 54.4 mm yr^{-1} that perfectly agrees with the prediction of the NZROT51 pole (54.6 ± 0.6 mm yr^{-1}). For the B site (lon: –78.78° and lat: –12.38°: Peru trench), the average velocity of 61.7 mm yr^{-1} also agrees with the NZROT51 velocity (61.2 ± 0.7 mm yr^{-1}). Finally, the average velocity at the C site

(lon: –72.57°, lat: –31.0°) is 66.9 mm yr^{-1}, a value at the upper bounds of the NZROT51 prediction (65.4 mm yr^{-1}). All models further agree with ∼5° in direction. In conclusion, NZROT51 pole agrees at the 1 mm accuracy with respect to previous Euler pole estimates.

5.2 San Felix

We did not include campaign results published by Kendrick *et al.* (2003) for San Felix (FLIX) and Robinson Crusoe (RBSN) islands in our calculations, because different ITRF and a different realization of the South America Plate fixed frame were used. The analysis shown for EISL also indicates that velocities estimated using data collected in the 1990s might have 1–2 mm yr^{-1} differences compared to velocity determined using post-2000 data. It is, however, informative to check our results against the published values and make some predictions to be compared to future estimates. San Felix island is located ∼800 km from the Chilean trench, in front of a segment ruptured by a great earthquake a century ago (Ruiz & Madariaga 2018). No tectonic deformation is suspected in that area, making San Felix an ideal site to determine the rigid motion of the Nazca Plate.

Our preferred solution prediction at FLIX is 64.5 ± 0.5 and 6.9 ± 0.5 mm yr^{-1} for the east and north components, respectively. This prediction is 1.6 ± 0.4 mm yr^{-1} faster than the observed velocity estimated by Kendrick *et al.* (2003). We believe that this difference is consistent with a more realistic uncertainty than
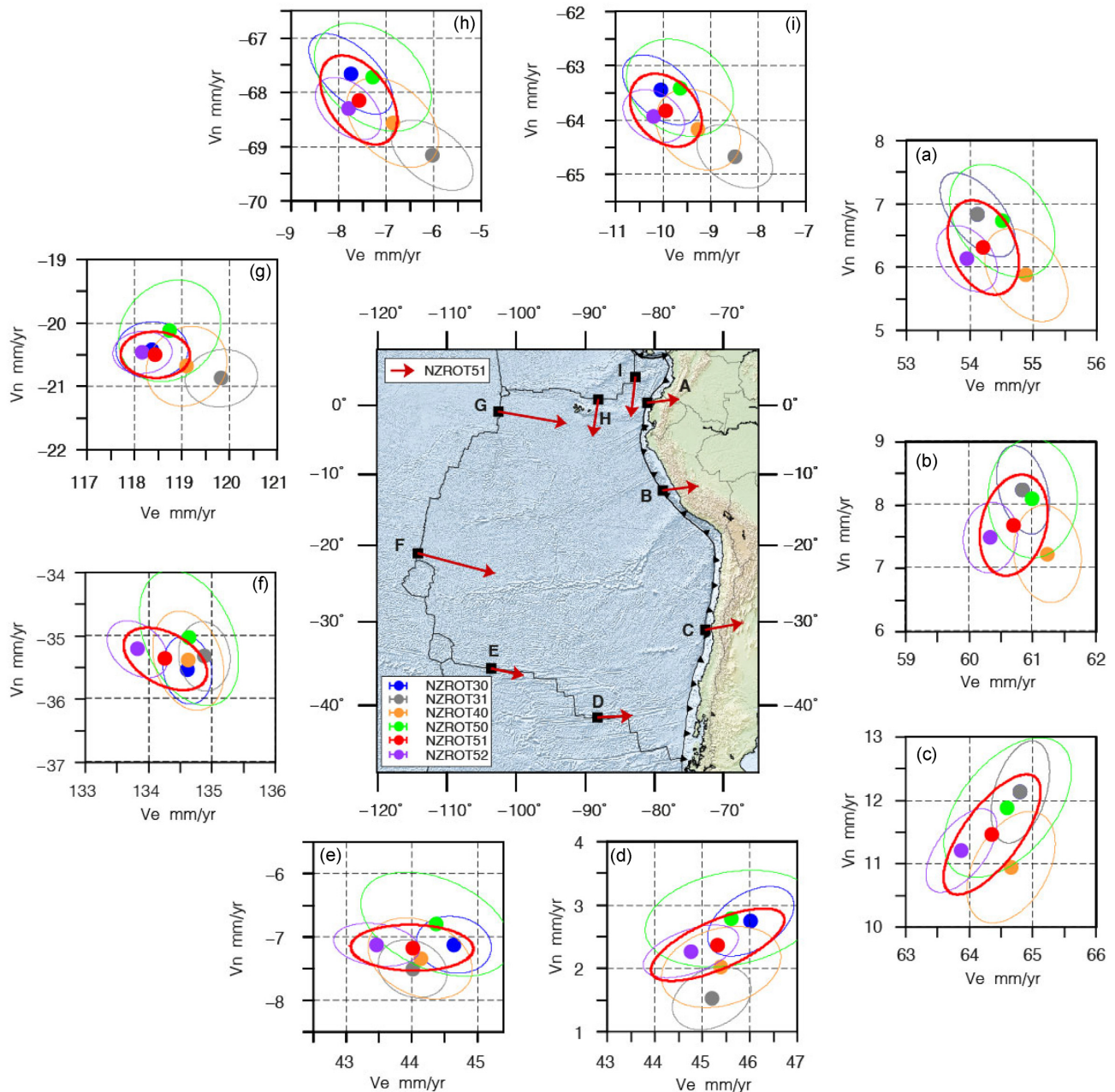
Figure 12. Predicted velocities from the six Nazca Euler poles summarized in Table 2. The map shows the selected locations along the Nazca Plate boundary indicated by black squares labeled from A to I. Red arrows show the velocity predicted by model NZROT51 for the Nazca Plate with respect to the adjacent plate. The subplots (a) to (i) show the prediction for the different Euler poles, together with their error ellipse at the 95 per cent confidence level for locations A to I.

the one reported (0.2 mm yr^{-1} for both components) in Kendrick *et al.* (2003).

We further evaluate the improvement expected from adding a well-defined velocity at the 0.5 mm yr^{-1} level at San Felix Island. The availability of new measurements at San Felix would significantly improve the spatial sampling of the Nazca Plate and would allow a precise test of potential internal deformation with respect to Salas y Gomez/Easter Islands. As an exercise adding a fictive measurement at San Felix, we find that the formal variance for the rotation rate for the Nazca Plate would be decreased by 50 per cent and the uncertainty in the convergence along the Chilean trench would

be improved by ∼35 per cent (0.5 mm yr^{-1} versus 0.8 mm yr^{-1} for our solution). Therefore, continuous GNSS measurements at San Felix appear as a priority to improve the Nazca current Plate kinematics description.

5.3 Convergence along the Andean margin

Fig. 13 shows the magnitude and direction for the convergence of the Nazca Plate with respect to South America along the trench from Colombia to Chile for previously published Euler poles and
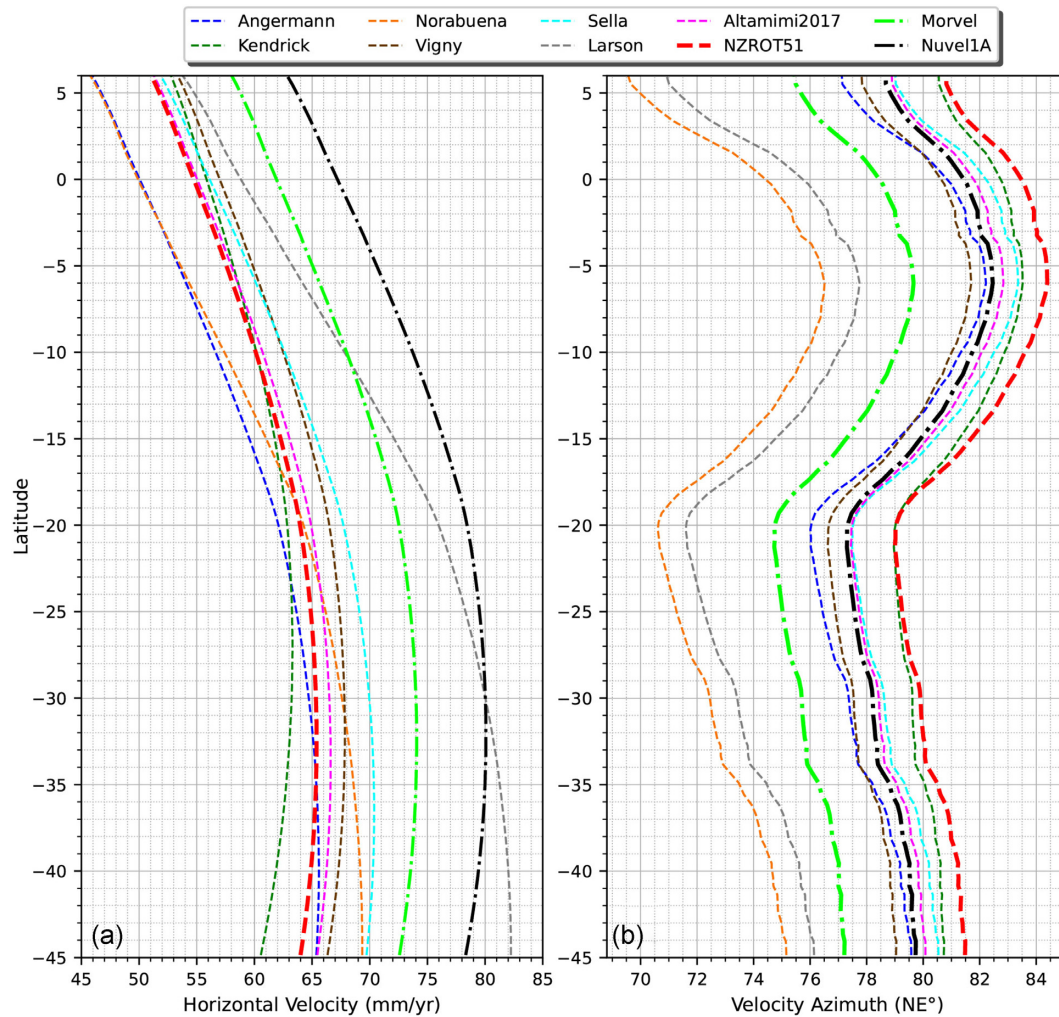
Figure 13. (a) Predicted velocity norm and (b) predicted directions along the NAZCA–SOAM Plate boundary according to our preferred model NZROT51, Larson *et al.* (1997), Angermann *et al.* (1999), Norabuena *et al.* (1999), Sella *et al.* (2002), Kendrick *et al.* (2003), Vigny *et al.* (2009), Altamimi *et al.* (2017), DeMets *et al.* (1994) and DeMets *et al.* (2010).

our preferred solution. Our model predicts ∼51 mm yr⁻¹ of convergence in northern Colombia, increasing to ∼58 mm yr⁻¹ at the convex bend of the trench at latitude 5°S. The convergence rate along the Peru trench increases from ∼58 mm yr⁻¹ in northern Peru to 64 mm yr⁻¹ in its southern part. Aside the oldest models from Larson *et al.* (1997), Angermann *et al.* (1999) and Norabuena *et al.* (1999), the difference among model predictions is less than 2 mm yr⁻¹ for the northern Andes. Differences increase in southern Peru and are largest along the Chilean trench where our model predicts a maximum convergence rate of 65.5 mm yr⁻¹ at latitude ∼30°S in Chile, falling in the middle of the fastest model from Vigny *et al.* (2009) at 68 mm yr⁻¹ and the slowest model of Kendrick *et al.* (2003) at 63 mm yr⁻¹. The predicted convergence azimuths are usually similar within 5° for all models (except for Larson *et al.* 1997; Norabuena *et al.* 1999), but our model prediction is systematically rotated by a few degrees clockwise with respect to the other models. Overall, our model is close to Altamimi *et al.* (2017), but with ∼1 mm yr⁻¹ slower convergence in front of Chile. Furthermore, the obliquity of the predicted convergence vectors along the whole trench axis (Fig. 14) appears consistent with the lateral motion found for continental slivers along the Andean margin (Wang

et al. 2007; Brooks *et al.* 2003; Métois *et al.* 2013; Nocquet *et al.* 2014).

5.4 Constant slowdown of Nazca motion for 3.16 Ma

The progressive slowdown of Nazca eastward motion has been well-documented from both geological and geodetic results (Norabuena *et al.* 1999; DeMets *et al.* 2010). Among the best evidence, DeMets *et al.* (2010) indicate that for Antarctic–Nazca spreading centres, located west and east of the Valdavia transform fault (longitude 84–92°W, latitude 41.5°S), opening rates decrease from 57 to 58 mm yr⁻¹ for the 3.16 Myr average motion in NUVEL1A, down to 50–52 mm yr⁻¹ for the 0.78 Myr average in MORVEL. Combining our preferred Nazca pole with the one from Altamimi *et al.* (2017) for the Antarctic Plate, we find an Euler pole at –92.038°E 39.246°N 0.414 deg Myr⁻¹ for the current Nazca–Antarctic Plate, predicting opening rates at 44–46 mm yr⁻¹ at the same location. Such values confirm the ongoing slowdown of opening rate along the Nazca–Antarctic Plate boundary. We can further quantitatively test whether our geodetic estimates agree with a constant deceleration rate since 3.16 Ma. For that, we note that for a linear function,
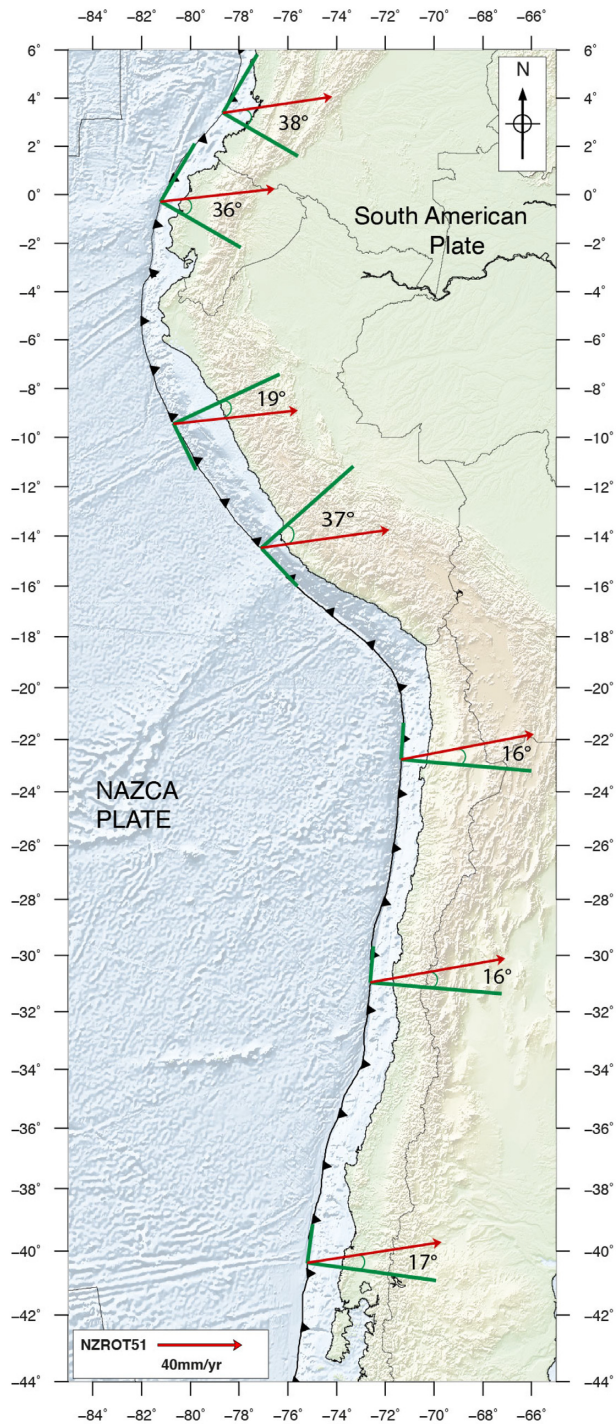
Figure 14. Convergence obliquity predicted by model NZROT51. Green lines indicate parallel and normal trench components of the Nazca–SOAM convergence vectors (red arrows).

the average rate over a given period is the value of the function at the middle time of the period. Therefore, under the assumption of constant slowdown, 3.16 Myr average motion in NUVEL1A provides the instantaneous opening rate at 3.16/2 Ma and MORVEL at 0.78/2 Ma. We use the full variance–covariance matrix provided with the NUVEL1 and MORVEL models and use the variance propagation law to obtain the velocity uncertainty at a given location. For the geodetic plate model, we add the variance–covariance of

our Nazca pole with the variance–covariance provided by Altamimi *et al.* (2017) for the Antarctic Plate to get the variance-covariance for the relative Nazca–Antarctic rotation vector. We choose two test locations at $M = (94.06°W, 38.00°S)$ and $N = (82.37°W, 43.90°S)$ where numerous spreading rates provide direct observations of the relative Nazca–Antarctic motion included in the NUVEL1 and MORVEL models (DeMets *et al.* 2010). Along these spreading centres, MORVEL predictions for the Nazca–Antarctic motion are rotated by 5° clockwise with respect to NUVEL1A predictions and the geodetic Nazca–Antarctic model prediction is rotated by 2–3° with respect to MORVEL. We neglect these small rotations and directly use the norm of the opening rate in the following calculations. At location M, we find opening rates of 59.5 ± 1.9 mm yr^{-1} for NUVEL1A, 50.2 ± 1.3 mm yr^{-1} for MORVEL and 44.9 ± 0.7 mm yr^{-1} for geodesy. Using these values and their associated uncertainty, we solve for a constant deceleration rate and present-day opening rate using weighted least-squares. We find that a deceleration rate of 9.5 ± 1.2 mm yr^{-1} per Myr and a present-day velocity of 45.2 ± 0.7 mm yr^{-1} provides a fit with residuals <1.1 mm yr^{-1}. The same calculation at location N, opening rates decrease from 61.3 ± 2.0 for NUVEL1A, 51.6 ± 1.3 for MORVEL and 45.7 ± 0.8 for geodesy. The best deceleration rate is found for 10.2 ± 1.3 mm yr^{-1} per Myr and residuals are less than 1.5 mm yr^{-1}, a value consistent with the standard deviation of the spreading rates.

Therefore, our pole is consistent with a constant ~1 cm yr^{-1} per Myr deceleration of opening rates along the Nazca–Antarctic boundary for 3.16 Ma. As for the MORVEL model, combining the Euler pole from Altamimi *et al.* (2017) for the Antarctic and Pacific plates with our pole for the Nazca pole, a Nazca–Pacific–Antarctic Plate circuit closure test shows insignificant residual (~1 mm yr^{-1}) supporting the plate rigidity hypothesis.

Several competing models have been proposed to explain the slowdown in the eastward motion of the Nazca Plate for the last ~20 Myr. A first group of models suggests the slowdown could be mainly attributed to the growth of the Andean cordillera at the western edge of South America. Increasing topographic load gradually increased frictional stresses on the plate interface, hence enhancing resistance to the Nazca Plate subduction (Norabuena *et al.* 1999; Iaffaldano *et al.* 2006; Meade & Conrad 2008). Martinod *et al.* (2010) also argue that flat-slab segments developed since the Eocene beneath North-Central Peru and North-Central Chile because of the subduction of more buoyant oceanic plateaus. Flat-slab development is proposed to have controlled the Andes growth and to have reduced the convergence velocity through increased interplate coupling. A second group of models invoke marge-scale mantle processes as a cause for change in plate motion. For instance, numerical models from Quinteros & Sobolev (2013) find that the Nazca subduction slowdown might result from increased resistance as the Nazca slab reaches the more viscous lower mantle, possibly during the late Eocene. Silver *et al.* (1998) alternatively find that a major plate motion re-organization occurred 30 Ma because of Africa northward motion slowdown. This resulted in a change in the mantle flow, leading to accelerated South America trenchward motion and shortening developing along the Andes. Possibly, this reorganization was an even larger-scale process also involving the progressive slowdown of the Nazca–South America and Nazca–Antarctic motion.

5.5 Northern Nazca Plate

At the northern part of the Nazca Plate, our analysis does not support the hypothesis of the independent Malpelo microplate proposed by

Zhang *et al.* (2017). Indeed, Zhang *et al.* (2017) relative motion between the Nazca Plate and Malpelo microplate is expected to be 5–6 mm yr^{-1} while cGPS site MALO at Malpelo Island shows a residual velocity always less than 1.5 mm yr^{-1} in our Nazca Euler pole estimations.

We test whether our new solution improves the misfit found in the MORVEL model for the Pacific–Cocos–Nazca Plate circuit closure. Using the MORVEL Cocos–Pacific Euler pole together with the geodetic poles for the Pacific Plate from Altamimi *et al.* (2017) and our pole for the Nazca Plate, we obtain a linear velocity of non-closure by 9.7 ± 2.1 mm yr^{-1} (evaluated at location: –102.0°E, 2.3°N) at the 95 per cent confidence level for the Pacific–Cocos–Nazca Plate circuit. This value is 30 per cent better than MORVEL, but only 17 per cent better than Zhang *et al.* (2017) estimates, without the need of an additional plate though.

Our solution includes cGPS site ISCO located on the Cocos Island. ISCO horizontal velocity is ($Ve = 54.35$ and $Vn = 64.25$ mm yr^{-1}) in the South American reference frame and ($Ve = 3.7$ and $Vn = 61.8$ mm yr^{-1}) with respect to the Nazca Plate using our solution. At the ISCO location, MORVEL prediction for the Cocos Plate motion in a Nazca fixed frame is ($Ve = -1.8$, and $Vn = 59.0$ mm yr^{-1}). Thus, there is a discrepancy of ∼6 mm yr^{-1} mainly on the east component between MORVEL prediction and the only available geodetic observation of Cocos–Nazca plates relative motion. Interestingly, we note that this discrepancy would be reduced by applying a decrease of the east component of the Nazca Plate similar to the one observed in its southern part. Noting the potentially biased Cocos kinematics in MORVEL, DeMets *et al.* (2010) propose an alternative Euler pole called PVEL for the Cocos–North America and Cocos–Caribbean plates. Using their values for the Cocos–North America pole, together with Altamimi *et al.* (2017) for the North America–South America kinematics and our Nazca–South America poles, the predicted velocity for PVEL at ISCO relative to Nazca is ($Ve = 9.9$ and $Vn = 68.4$ mm yr^{-1}), leading to a 9 mm yr^{-1} difference with our estimate. Given the overall consistency of cGPS velocities in the Galapagos archipelago and Malpelo Island, the consistency of these velocities with cGPS sites at Easter Island and Salas y Gomez Island, it is likely that errors in the kinematics of the Cocos Plate is the main contribution to the large misfit observed in MORVEL for the Pacific–Cocos–Nazca Plate circuit closure.

6 CONCLUSIONS

Despite the limited number of available continuous GPS observations within the plate, our study has allowed us to better constrain the kinematics of the Nazca Plate by reducing the uncertainties of previous pole estimates. Our best estimate for the Nazca Plate Euler pole (NZROT51: long. –90.93°E, lat. 56.19°, $\omega = 0.588$ deg Myr^{-1}) is defined by five sites sampling a wide area of the plate.

Analysis of potential volcanic and tectonic deformation shows that ILSG at Salas y Gomez Island and SCEC in the easternmost island of the Galapagos archipelago are the most stable sites within the plate. Easter Island, Santa Cruz Island in the Galapagos, and Malpelo Island offshore Colombia probably undergo deformation at the 1–2 mm yr^{-1} level. Robinson Crusoe Island experiences viscoelastic effects of the large earthquakes along the Chile subduction zone, biasing velocity estimates at 4–5 mm yr^{-1} for the next years and possibly decades. In the absence of seafloor geodesy measurements, confirmation or re-evaluation of the Nazca present-day

kinematics is expected to depend on a reliable velocity estimate at San Felix Island located ∼800 km from the Chile trench.

New GPS measurements at Malpelo Island do not support the existence of an independent Malpelo microplate in the northernmost part of the Nazca Plate. On the contrary, our analysis supports a single plate with possible internal deformation of the order of 0.6 mm yr^{-1}, a residual similar to other large tectonic plates when correcting velocities from geophysical models. This indicates very small, if any, contribution of thermal contraction of the oceanic lithosphere previously proposed (Kumar & Gordon 2009). The misfit of the Pacific–Cocos–Nazca Plate circuit closure appears to be reduced but not solved by our Nazca pole. However, the good agreement of geodetic velocity with the plate rigidity assumption for a large area of the Nazca Plate sampled by geodetic velocity points makes internal deformation or fragmentation of the Nazca Plate unlikely as possible explanations. A combination of fast slowdown of the Nazca Plate and bias in the Cocos Plate kinematics appears to be a more probable explanation for the Cocos–Pacific–Nazca Plate circuit non-closure issue.

DATA AVAILABILITY

GPS velocities are provided in the paper and in the Supporting Information. Additional data related to this paper may be requested from the corresponding author. GPS data are available online though Unavco interface (https://www.unavco.org/data), Instituto Geográafico Militar of Ecuador (http://www.geoportaligm.gob.ec), Red Argentina de Monitoreo Satelital Continuo https://www.ign.gob.ar and Centro Sismológico Nacional (http://gps.csn.uchile.cl). Earthquake catalogue and focal mechanism solutions were downloaded from the International Seismological Centre (ISC) and the Global Centroid Moment Tensor (gCMT).

REFERENCES

Adamek, S., Frohlich, C. & Pennington, W.D., 1988. Seismicity of the Caribbean-Nazca boundary: constraints on microplate tectonics of the Panama region, *J. geophys. Res.,* **93,** 2053–2075.

Altamimi, Z., Métivier, L. & Collilieux, X., 2012. ITRF2008 plate motion model, *J. geophys. Res.,* **117,** doi:10.1029/2011JB008930.

Altamimi, Z., Métivier, L., Rebischung, P., Rouby, H. & Collilieux, X., 2017. ITRF2014 plate motion model, *Geophys. J. Int.,* **209,** 1906–1912.

Alvarado, A., *et al.*, 2018. Seismic, volcanic, and geodetic networks in Ecuador: building capacity for monitoring and research, *Seismol. Res. Lett.,* **89,** 432–439.

Amelung, F., Jónsson, S., Zebker, H. & Segall, P., 2000. Widespread uplift and trapdoor faulting on Galápagos volcanoes observed with radar interferometry, *Nature,* **407,** 993–996.

Angermann, D., Klotz, J. & Reigber, C., 1999. Space-geodetic estimation of the Nazca-South America Euler Vector, *Earth planet. Sci. Lett.,* **171,** 329–334.

Árnadóttir, T., Lund, B., Jiang, W., Geirsson, H., Björnsson, H., Einarsson, P. & Sigurdsson, T., 2009. Glacial rebound and plate spreading: results from the first countrywide GPS observations in Iceland, *Geophys. J. Int.,* **177,** 691–716.

Báez, J.C., *et al.*, 2018. The Chilean GNSS network: current status and progress toward early warning applications, *Seismol. Res. Lett.,* **89,** 1546–1554.

Bagnardi, M. & Amelung, F., 2012. Space-geodetic evidence for multiple magma reservoirs and subvolcanic lateral intrusions at Fernandina Volcano, Galápagos Islands, *J. geophys. Res.,* **117** , doi:10.1029/2012JB009465.

Baker, M.S., 2012. Investigating the dynamics of basaltic volcano magmatic systems with space geodesy,, *PhD thesis*, University of Miami, Coral Gables, FL, USA, Retrieved from https://scholarlyrepository.miami.edu/oa_dissertations/917.

Behn, M.D. & Ito, G., 2008. Magmatic and tectonic extension at mid-ocean ridges: 1. Controls on fault characteristics, *Geochem. Geophys. Geosyst.,* **9,** doi:10.1029/2008GC001965.

Bevis, M. & Brown, A., 2014. Trajectory models and reference frames for crustal motion geodesy, *J. Geod.,* **88,** 283–311.

Blewitt, G., Hammond, W. & Kreemer, C., 2018. Harnessing the GPS data explosion for interdisciplinary science, *EOS,* **99** , doi:10.1029/2018EO104623.

Blewitt, G. & Lavallée, D., 2002. Effect of annual signals on geodetic velocity, *J. geophys. Res.,* **107,** ETG9–1-ETG9-11.

Boehm, J., Werl, B. & Schuh, H., 2006. Troposphere mapping functions for GPS and very long baseline interferometry from European Centre for medium-range weather forecasts operational analysis data, *J. geophys. Res.,* **111** , doi:10.1029/2005JB003629.

Bos, M. S., Fernandes, R.M.S., Williams, S.D.P. & Bastos, L., 2013. Fast error analysis of continuous GNSS observations with missing data, *J. Geod.,* **87,** 351–360.

Bos, M.S. & Fernandes, R.M.S., 2015. Investigation of random walk noise in GNSS time-series, in *Presented at the 2015 AGU Fall Meeting,* Abstract ID G13A-0990, AGU. Retrieved from https://agu.confex.com/agu/fm15/meetingapp.cgi/Paper/73901.

Brooks, B.A., *et al.*, 2003. Crustal motion in the Southern Andes (26°–36°S): do the Andes behave like a microplate?, *Geochem., Geophys., Geosyst.,* **4,** doi:10.1029/2003GC000505.

Chadwick, W.W. Jr., Geist, D.J., Jónsson, S., Poland, M., Johnson, D.J. & Meertens, C.M., 2006. A volcano bursting at the seams: inflation, faulting, and eruption at Sierra Negra volcano, Galápagos, *Geology,* **34,** 1025–1028.

Delouis, B., Nocquet, J.-M. & Vallée, M., 2010. Slip distribution of the February 27, 2010 Mw = 8.8 Maule Earthquake, central Chile, from static and high-rate GPS, InSAR, and broadband teleseismic data, *Geophys. Res. Lett.,* **37**(17), doi:10.1029/2010GL043899.

DeMets, C., Gordon, R.G., Argus, D.F. & Stein, S., 1994. Effect of recent revisions to the geomagnetic reversal time scale on estimates of current plate motions, *Geophys. Res. Lett.,* **20**(21), 2191–2194.

DeMets, C., Gordon, R.G. & Argus, D.F., 2010. Geologically current plate motions, *Geophys. J. Int.,* **181,** 1–80.

Di Giacomo, D., Bondár, I., Storchak, D.A., Engdahl, E.R., Bormann, P. & Harris, J., 2015. ISC-GEM: Global Instrumental Earthquake Catalogue (1900–2009), III. Re-computed MS and mb, proxy MW, final magnitude composition and completeness assessment, *Phys. Earth planet. Inter.,* **239,** 33–47.

Dow, J.M., Neilan, R.E. & Rizos, C., 2009. The International GNSS Service in a changing landscape of Global Navigation Satellite Systems, *J. Geod.,* **83,** 191–198.

Ekström, G., Nettles, M. & Dziewoński, A.M., 2012. The global CMT project 2004–2010: centroid-moment tensors for 13,017 earthquakes, *Phys. Earth planet. Inter.,* **200–201,** 1–9.

Engdahl, E.R., Di Giacomo, D., Sakarya, B., Gkarlaouni, C.G., Harris, J. & Storchak, D.A., 2020. ISC-EHB 1964–2016, an improved data set for studies of earth structure and global seismicity, *Earth Space Sci.,* **7,** doi:10.1029/2019EA000897.

Engeln, J.F. & Stein, S., 1984. Tectonics of the Easter plate, *Earth planet. Sci. Lett.,* **68,** 259–270.

Galetto, F., Bagnardi, M., Acocella, V. & Hooper, A., 2019. Noneruptive unrest at the Caldera of Alcedo Volcano (Galápagos Islands) revealed by InSAR data and geodetic modeling, *J. geophys. Res.,* **124**(4), 3365–3381.

Geist, D.J., Harpp, K.S., Naumann, T.R., Poland, M., Chadwick, W.W., Hall, M. & Rader, E., 2008. The 2005 eruption of Sierra Negra volcano, Galápagos, Ecuador, *Bull. Volcanol.,* **70,** 655–673.

Griffiths, J., 2019. Combined orbits and clocks from IGS second reprocessing, *J. Geod.,* **93,** 177–195.

Herring, T.A., Floyd, M.A., King, R.W. & McClusky, S.C., 2015. *Global Kalman Filter VLBI and GPS Analysis Program Release 10.6,* pp. 95, MIT.

Herring, T.A., King, R.W., Floyd, M.A. & McClusky, S.C., 2018. *GPS Analysis at MIT Release 10.7 (No. Release 10.7),* MIT.

Johnston, G., Riddell, A. & Hausler, G., 2017. The International GNSS Service, in *Springer Handbook of Global Navigation Satellite Systems,* 1st edn, pp. 967–982, eds Teunissen, P.J. & Montenbruck, O., Springer International Publishing.

Iaffaldano, G., Bunge, H.-P. & Dixon, T.H., 2006. Feedback between mountain belt growth and plate convergence, *Geology,* **34,** 893–896.

Kanamori, H. & McNally, K.C., 1982. Variable rupture mode of the subduction zone along the Ecuador-Colombia coast, *Bull. seism. Soc. Am.,* **72,** 1241–1253.

Kendrick, E., Bevis, M., Smalley, R., Brooks, B., Vargas, R.B., Lauriá, E. & Fortes, L.P.S., 2003. The Nazca–South America Euler vector and its rate of change, *J. S. Am. Earth Sci.,* **16,** 125–131.

Khazaradze, G., Wang, K., Klotz, J., Hu, Y. & He, J., 2002. Prolonged post-seismic deformation of the 1960 great Chile earthquake and implications for mantle rheology, *Geophys. Res. Lett.,* **29,** 7–1, doi:10.1029/2002GL015986.

Klein, E., Fleitout, L., Vigny, C. & Garaud, J.D., 2016. Afterslip and viscoelastic relaxation model inferred from the large-scale post-seismic deformation following the 2010 Mw 8.8 Maule earthquake (Chile), *Geophys. J. Int.,* **205,** 1455–1472.

Kobayashi, D., LaFemina, P., Geirsson, H., Chichaco, E., Abrego, A.A., Mora, H. & Camacho, E., 2014. Kinematics of the western Caribbean: collision of the Cocos Ridge and upper plate deformation, *Geochem. Geophys. Geosyst.,* **15,** 1671–1683.

Kruse, S.E., Liu, Z.J., Naar, D.F. & Duncan, R.A., 1997. Effective elastic thickness of the lithosphere along the Easter Seamount Chain, *J. geophys. Res.,* **102,** 27 305–27 317.

Kumar, R.R. & Gordon, R.G., 2009. Horizontal thermal contraction of oceanic lithosphere: the ultimate limit to the rigid plate approximation, *J. geophys. Res.,* **114,** doi:10.1029/2007JB005473.

Larson, K.M., Freymueller, J.T. & Philipsen, S., 1997. Global plate velocities from the Global Positioning System, *J. geophys. Res.,* **102,** 9961–9981.

Liu, Z., 1996. The Origin and Evolution of the Easter Seamount Chain, *PhD thesis*, University of South Florida, Retrieved from https://books.google.fr/books?id=w8kPAQAAIAAJ.

Lonsdale, P., 2005. Creation of the Cocos and Nazca plates by fission of the Farallon plate, *Tectonophysics,* **404,** 237–264.

Lonsdale, P. & Klitgord, K.D., 1978. Structure and tectonic history of the eastern Panama Basin, *GSA Bull.,* **89,** 981–999.

Lyard, F., Lefevre, F., Letellier, T. & Francis, O., 2006. Modelling the global ocean tides: modern insights from FES2004, *Ocean Dyn.,* **56,** 394–415.

Marcaillou, B., Charvis, P. & Collot, J.-Y., 2006. Structure of the Malpelo Ridge (Colombia) from seismic and gravity modelling, *Mar. Geophys. Res.,* **27,** 289–300.

Martinod, J., Husson, L., Roperch, P., Guillaume, B. & Espurt, N., 2010. Horizontal subduction zones, convergence velocity and the building of the Andes, *Earth planet. Sci. Lett.,* **299,** 299–309.

Mccaffrey, R., 2002. Crustal block rotations and plate coupling, in *Plate Boundary Zones,* pp. 101–122, American Geophysical Union, doi:10.1029/GD030p0101.

McCarthy, D., 1996. IERS Conventions (1996), *Technical Note 21, Observatory of Paris: IERS,* Retrieved from https://www.iers.org/IERS/EN/Publications/TechnicalNotes/tn21.html.

Meade, B. J. & Hager, B., 2005. Block models of crustal motion in southern California constrained by GPS measurements, *J. geophys. Res.,* **110**(B3), doi:10.1029/2004JB003209.

Meade, B.J., 2007. Algorithms for the calculation of exact displacements, strains, and stresses for triangular dislocation elements in a uniform elastic half space, *Comput. Geosci.,* **33,** 1064–1075.

Meade, B.J. & Conrad, C.P., 2008. Andean growth and the deceleration of South American subduction: Time evolution of a coupled orogen-subduction system, *Earth planet. Sci. Lett.,* **275,** 93–101.

Métois, M., Socquet, A., Vigny, C., Carrizo, D., Peyrat, S., Delorme, A., Maureira, E., *et al.*, 2013. Revisiting the North Chile seismic gap segmentation using GPS-derived interseismic coupling, *Geophys. J. Int.,* **194,** 1283–1294.

Mishra, J.K. & Gordon, R.G., 2016. The rigid-plate and shrinking-plate hypotheses: implications for the azimuths of transform faults, *Tectonics,* **35,** 1827–1842.

Mooney, W., 2015. Crust and lithospheric structure - global crustal structure, in *Treatise on Geophysics,* Vol. **1,** pp. 339–372, ed. Schubert, G., Elsevier B.V.

Mora-Páez, H., Kellogg, J.N., Freymueller, J.T., Mencin, D., Fernandes, R.M.S., Diederix, H., LaFemina, P., *et al.*, 2019. Crustal deformation in the northern Andes – a new GPS velocity field, *J. S. Am. Earth Sci.,* **89,** 76–91.

Mora-Páez, H., *et al.*, 2018. Space geodesy infrastructure in colombia for geodynamics research, *Seismol. Res. Lett.,* **89,** 446–451.

Mothes, P.A., Nocquet, J.-M. & Jarrín, P., 2013. Continuous GPS network operating throughout Ecuador, *EOS, Trans. Am. geophys. Un.,* **94,** 229–231.

Nocquet, J.-M., Calais, E., Altamimi, Z., Sillard, P. & Boucher, C., 2001. Intraplate deformation in western Europe deduced from an analysis of the International Terrestrial Reference Frame 1997 (ITRF97) velocity field, *J. geophys. Res.,* **106,** 11 239–11 257.

Nocquet, J.-M., 2002. Mesure de la déformation crustale en Europe occidentale par géodésie spatiale, *PhD thesis,* University of Nice Sophia Antipolis, Nice, 307 pp.

Nocquet, J.-M., *et al.*, 2016. Supercycle at the Ecuadorian subduction zone revealed after the 2016 Pedernales earthquake, *Nat. Geosci.,* **10,** 145, doi:10.1038/ngeo2864.

Nocquet, J.-M., *et al.*, 2014. Motion of continental slivers and creeping subduction in the northern Andes, *Nat. Geosci.,* **7,** 287–291.

Nocquet, J.-M., 2012. Present-day kinematics of the Mediterranean: a comprehensive overview of GPS results, *Tectonophysics,* **579,** 220–242.

Norabuena, E.O., Dixon, T.H., Stein, S. & Harrison, C.G.A., 1999. Decelerating Nazca-South America and Nazca-Pacific Plate motions, *Geophys. Res. Lett.,* **26,** 3405–3408.

Pennington, W.D., 1981. Subduction of the Eastern Panama Basin and seismotectonics of northwestern South America, *J. geophys. Res.,* **86,** 10 753–10 770.

Perfit, M.R. & Chadwick, W.W. Jr, 1998. Magmatism at Mid-Ocean Ridges: constraints from volcanological and geochemical investigations, in *Faulting and Magmatism at Mid-Ocean Ridges,* pp. 59–115, American Geophysical Union, doi:10.1029/GM106p0059.

Piñón, D.A., Gómez, D.D., Smalley, R. Jr, Cimbaro, S.R., Lauría, E.A. & Bevis, M.G., 2018. The history, state, and future of the argentine continuous satellite monitoring network and its contributions to geodesy in Latin America, *Seismol. Res. Lett.,* **89,** 475–482.

Prawirodirdjo, L. & Bock, Y., 2004. Instantaneous global plate motion model from 12 years of continuous GPS observations, *J. geophys. Res.,* **109,** doi:10.1029/2003JB002944.

Quinteros, J. & Sobolev, S.V., 2013. Why has the Nazca plate slowed since the Neogene?, *Geology,* **41,** 31–34.

Rebischung, P., Altamimi, Z., Ray, J. & Garayt, B., 2016. The IGS contribution to ITRF2014, *J. Geod.,* **90,** 611–630.

Rodrigo, C., Diaz, J. & Gonzalez-Fernandez, A., 2014. Origin of the Easter Submarine Alignment: morphology and structural lineaments, *Latin Am. J. Aquat. Res.,* **42,** 857–870.

Ruiz, S. & Madariaga, R., 2018. Historical and recent large megathrust earthquakes in Chile, *Tectonophysics,* **733,** 37–56.

Sella, G.F., Dixon, T.H. & Mao, A., 2002. REVEL: a model for Recent plate velocities from space geodesy, *J. geophys. Res.,* **107,** ETG 11–1-ETG 11-30.

Silver, P.G., R., M. Russo & Lithgow-Bertelloni, C., 1998. Coupling of South American and African plate motion and plate deformation, *Science,* **279,** 60–63.

Suito, H. & Freymueller, J., 2009. A viscoelastic and afterslip postseismic deformation model for the 1964 Alaska earthquake, *J. geophys. Res.,* **114,** doi:10.1029/2008JB005954.

Trenkamp, R., Kellogg, J.N., Freymueller, J.T. & Mora, H.P., 2002. Wide plate margin deformation, southern Central America and northwestern South America, CASA GPS observations, *J. S. Am. Earth Sci.,* **15,** 157–171.

UNAVCO Community, 2008. COCONet GPS Network - Station CN00 and 45 Others, The GAGE Facility operated by UNAVCO, Inc., GPS/GNSS Observations (Aggregation of Multiple Datasets)

Vezzoli, L. & Acocella, V., 2009. Easter Island, SE Pacific: an end-member type of hotspot volcanism, *GSA Bull.,* **121,** 869–886.

Vigny, C., *et al.*, 2011. The 2010 Mw 8.8 Maule megathrust earthquake of Central Chile, monitored by GPS, *Science,* **332,** 1417, doi:10.1126/science.1204132.

Vigny, C., Rudloff, A., Ruegg, J.-C., Madariaga, R., Campos, J. & Alvarez, M., 2009. Upper plate deformation measured by GPS in the Coquimbo Gap, Chile, *Phys. Earth planet. Inter.,* **175,** 86–95.

Wang, K., Hu, Y., Bevis, M., Kendrick, E., Smalley, R. Jr, Vargas, R.B. & Lauría, E., 2007. Crustal motion in the zone of the 1960 Chile earthquake: detangling earthquake-cycle deformation and forearc-sliver translation, *Geochem. Geophys. Geosyst.,* **8** , doi:10.1029/2007GC001721.

White, S.M., Trenkamp, R. & Kellogg, J.N., 2003. Recent crustal deformation and the earthquake cycle along the Ecuador–Colombia subduction zone, *Earth planet. Sci. Lett.,* **216,** 231–242.

Williams, S.D.P., 2008. CATS: GPS coordinate time series analysis software, *GPS Solut.,* **12,** 147–153.

Ye, L., Kanamori, H., Avouac, J.-P., Li, L., Cheung, K.F. & Lay, T., 2016. The 16 April 2016, MW7.8 (MS7.5) Ecuador earthquake: a quasi-repeat of the 1942 MS7.5 earthquake and partial re-rupture of the 1906 MS8.6 Colombia–Ecuador earthquake, *Earth planet. Sci. Lett.,* **454,** 248–258.

Zhang, T., Gordon, R.G., Mishra, J.K. & Wang, C., 2017. The Malpelo Plate Hypothesis and implications for nonclosure of the Cocos-Nazca-Pacific plate motion circuit, *Geophys. Res. Lett.,* **44,** 8213–8218.

SUPPORTING INFORMATION

Supplementary data are available at *GJI* online.

Figure S1. Top panel: daily position (north and east components) time-series for EISL site (Easter Island, Chile). In order to evaluate their consistency, the best-fitting velocity from site ISPA, located ∼4 km from EISL, has been removed from EISL raw time-series (north = –11.3 mm yr^{-1}, east = 64.8 mm yr^{-1}). Light pink stripe highlights the period (2001–2003.1) of abnormal trend. The red curve shows the best trajectory model estimated for the 1994–2004.5 period. The orange curve is our final best-fitting velocity

model estimated for the 1996–2004.5 period and omitting the 2001–2003.1 period. Bottom panel: residual time-series with respect to our best-fitting trajectory model, obtained using the 1996–2004 and removing the data from the 2001–2003.1 period.

Figure S2. Top panel: daily position (north and east components) time-series for ISPA site (Easter Island, Chile). For visualization purposes, a conventional value of (–10.2, 58.3) mm yr^{-1}, equivalent to 90 per cent of the best velocity has been removed. The red curve shows the best-fitting model. Bottom panel: residual time-series with respect to the best-fitting trajectory model.

Figure S3. Top panel: daily position (north and east components) time-series for ILSG site (Salas y Gomez Island, Chile). For visualization purposes, a conventional value of (–8.6, 57.6) mm yr^{-1}, equivalent to 90 per cent of the best velocity has been removed. The red curve shows the best-fitting model. Bottom panel: residual time-series with respect to the best-fitting trajectory model.

Figure S4. Top panel: daily position (north and east components) time-series for GALA site (Santa Cruz Island, Galapagos, Ecuador). For visualization purposes, a conventional value of (1.4, 49.7) mm yr^{-1}, equivalent to 90 per cent of the best velocity has been removed. The light pink stripe highlights the period of transient displacement. The red curve shows the best-fitting model omitting this period. Bottom panel: residual time-series with respect to the best-fitting trajectory model.

Figure S5. Top panel: daily position (north and east components) time-series for GLPS site (Santa Cruz Island, Galapagos, Ecuador). For visualization purposes, a conventional value of (2.1, 49.0) mm yr^{-1}, equivalent to 90 per cent of the best velocity has been removed. Light pink stripes denote periods of major volcanic activity for Sierra Negra volcano. The red curve shows the best-fitting model, obtained after removing the periods highlighted in light pink. Bottom panel: residual time-series with respect to the best-fitting trajectory model.

Figure S6. Top panel: daily position (north and east components) time-series for SCEC site (San Cristopbal, Galapagos, Ecuador). For visualization purposes, a conventional value of (1.2, 49.4) mm yr^{-1}, equivalent to 90 per cent of the best velocity has been removed. The red curve shows the best-fitting model. Bottom figure: Residual time-series with respect to the best-fitting trajectory model.

Figure S7. Top panel: daily position (north and east components) time-series for MALO site (Malpelo Island, Colombia). For visualization purposes, a conventional value of (4.1, 47.8) mm yr^{-1},

equivalent to 90 per cent of the best velocity has been removed. The red curve shows the best-fitting model. Bottom panel: residual time-series with respect to the best-fitting trajectory model.

Figure S8. Top panel: daily position (north and east components) time-series for ARJF site (Juan Fernandez Island, Chile). For visualization purposes, a conventional value of (5.8, 63.0) mm yr^{-1}, equivalent to 90 per cent of the best velocity has been removed. The red curve shows the best-fitting model. Bottom panel: residual time-series with respect to the best-fitting trajectory model.

Figure S9. Power spectral densities (PSD) for EISL (grey curve) and ISPA (red curve) residual time-series. Blue solid lines are the best-fitting power-law plus white noise models.

Figure S10. Differences of velocity prediction from Angermann *et al*. (1999), Kendrick *et al*. (2003), Vigny *et al*. (2009) and Altamimi *et al*. (2017) with respect to NZROT51 prediction every 3° along the Nazca–SOAM Plate boundary.

Table S1. GPS Velocities expressed in the ITRF2014 reference frame. Longitude and Latitude in decimal degrees. *Ve* and *Vn* are east and north components of velocity in mm yr^{-1}. *SVe*, *SVn* are the associated uncertainties (1σ confidence level) in mm yr^{-1}.

Table S2. South America Euler pole parameters and associated uncertainty. *Wx*, *Wy*, *Wz* are rotation rates in the Geocentric coordinate system. R_ve and R_vn are east and north velocity residuals in mm yr^{-1}. S_ve and S_vn are formal errors of R_vE and R_vn. RN_ve and RN_vn are normalized residuals. RMS, root-mean-square of residuals. wrms, weighted-rms of residuals.

Table S3. Noise amplitudes and spectral indices estimated by CATS at EISL and ISPA sites. k: spectral index. WH: White noise in mm. According to *k* values, flicker noise is the dominant model in the power-law process (PL), which is expressed in mm yr$^{-1/4}$.

Table S4. Preferred Nazca–South America Euler pole (NZROT51) parameters and associated uncertainty. *Wx*, *Wy*, *Wz* are rotation rates in the Geocentric coordinate system. R_ve and R_vn are east and north velocity residuals in mm yr^{-1}. S_ve and S_vn are formal errors of R_vE and R_vn. RN_ve and RN_vn are normalized residuals.rms is the root-mean-square of residuals. wrms is the weighted-rms of residuals.

Please note: Oxford University Press is not responsible for the content or functionality of any supporting materials supplied by the authors. Any queries (other than missing material) should be directed to the corresponding author for the paper.